Formation Flying and Position Determination for a Space-Based Interferometer in GEO Graveyard Orbit

Jeffrey Stuart
Jet Propulsion Laboratory
California Institute of Technology
4800 Oak Grove Dr.
Pasadena, CA 91109
818-354-0071
jeffrey.r.stuart@jpl.nasa.gov

Angela Dorsey
Jet Propulsion Laboratory
California Institute of Technology
4800 Oak Grove Dr.
Pasadena, CA 91109
818-731-3696
angela.r.dorsey@jpl.nasa.gov

Farah Alibay
Jet Propulsion Laboratory
California Institute of Technology
4800 Oak Grove Dr.
Pasadena, CA 91109
818-354-2778
farah.alibay@jpl.nasa.gov

Nuno Filipe
Jet Propulsion Laboratory
California Institute of Technology
4800 Oak Grove Dr.
Pasadena, CA 91109
818-354-0748
nuno.filipe@jpl.nasa.gov

***Abstract*—Spacecraft formations enable a variety of mission concepts, from gravity reconstruction to extrasolar planet detection to heliophysics observatories. In particular, space-based radio interferometers can detect signals in frequency ranges that are absorbed by Earth's ionosphere or atmosphere. Furthermore, such formation missions are now feasible under constrained cost caps due to the growing availability of SmallSat components with spaceflight heritage that are compatible the CubeSat form-factor. Accordingly, we analyze a mission concept operating multiple SmallSats in a passive cluster to establish a space-based interferometer. The goal of this array is to reconstruct radio emissions associated with Coronal Mass Ejections (CMEs) from the Sun, giving us insight into the particle acceleration occurring during these events. This low-cost mission concept presents a number of unique challenges in regards to mission design and navigation, particularly the configuration of the spacecraft to optimize science return and the reconstruction of precise spacecraft-spacecraft separation values. After providing a brief overview of the mission concept, this paper presents several key features of the mission design and orbit determination strategy that enable this potential heliophysics mission.**

TABLE OF CONTENTS

1. INTRODUCTION

Spacecraft formation flying enables a wide variety of mission concepts, with one compelling application being space-based very-long baseline interferometry (VLBI). While there is an extensive literature on the design, guidance, and control of spacecraft formations [1], [2], and even entire textbooks on the subject [3], there have been relatively few operational examples of missions flying spacecraft in clustered formations (that is, close proximity, rather than extended constellations such as the Global Position System [GPS]). To date, the GRACE [4] and GRAIL [5] missions each flew a pair of spacecraft in tandem to map the gravity of the Earth and Moon, respectively. Likewise, the THEMIS mission flew multiple spacecraft in Earth-orbits of varying size and eccentricity [6]; the extended follow-on mission ARTEMIS transferred two of the THEMIS spacecraft to lunar libration point, and ultimately lunar-centric, orbits [7]. The Magnetospheric Multiscale (MMS) mission, one of the first true "cluster formation" missions, is comprised of 4 spacecraft in highly elliptical Earth-orbit studying the magnetic reconnections in Earth's magnetosphere [8]. One difficulty with formation operations is that most mission concepts require active control and reconfiguration of the formation in order to meet specified geometries. Furthermore, active cross-linking between the satellites is necessary to share scientific data and the tracking signals needed for precise relative positioning; such applications require extensive and robust on-board processing and often entails the automated detection of "signaling events". Furthermore, the cost of building and testing multiple spacecraft is often prohibitive for cost-constrained budgets, though the growing availability and capability of SmallSat technology has greatly reduced this hurdle and led to an explosion in the number of proposed formation missions [9].

Our mission concept proposes to place six SmallSats into a geosynchronous (GEO) graveyard orbit, that is, altitudes slightly above GEO where old spacecraft and boosters are placed for disposal, where they would fly in a passive cluster to establish a space-based interferometer. Each spacecraft would operate independently and transmit data only to the ground stations, reducing the complexity and cost of the mission. All relevant science and operational data would be processed using established ground-based capabilities, further simplifying the development process. This array would be used to image radio emissions associated with Coronal Mass Ejections (CMEs) from the Sun, giving us insight into the particle acceleration occurring during these events. By understanding this particle acceleration, we can better characterize the formation and evolution of these highly

978-1-5090-1613-6/17/31.00

energetic events, with implications for long-term prediction and mitigation strategies for hazardous space weather.

A number of unique challenges in regards to mission design and navigation are addressed to enable this low-cost mission concept. The spacecraft would be deployed as secondary payloads into the GEO graveyard, where they must first be navigated into the desired formation. Once in that formation, the spacecraft must be distributed between 1 and 10 km in the plane orthogonal to the Sun-line such that the baselines forming the interferometer enable reconstruction of the radio emissions. Furthermore, communication with the ground is limited to once per week and the spacecraft use unbalanced thrusters for momentum wheel desaturation, entailing additional constraints on the formation maintenance strategy. In addition to the requirements on formation design and station-keeping, the relative position knowledge of the spacecraft must be known to within 3 meters in order to enable images of CMEs to be reconstructed.

After providing a brief overview of the mission concept, this paper presents several key features of the mission design and orbit determination strategy, including: 1) the approach taken to establish the initial spacecraft formation and maintain the spacecraft position during the lifetime of the mission; 2) the method used to optimize the distribution of the spacecraft in the plane orthogonal to the Sun, thus maximizing science return; 3) use of GPS signals at GEO to meet the relative position knowledge requirement; and 4) an alternate positioning strategy using cross-links between the satellites wherein tracking information, but no science data, is transferred within the formation.

2. INTERFEROMETRIC MISSION CONCEPT

Space-based radio astronomical arrays can address a wide range of scientific questions, ranging from planetary and extrasolar planetary magnetospheres and particle acceleration at shocks in the solar wind and in astronomical sources to potentially searching for the signatures of the first stars.The KISS Study "Small Satellites: A Revolution in Space Science" identified a concept called RELIC that would study the energy transport from black holes in galaxies [10], and a forthcoming KISS Study will also illustrate how a constellation of small satellites could study the magnetic fields of extrasolar planets.Further, the NASA Space Technology Mission Directorate recently released a solicitation aimed at technology development toward many aspects of cross-linked constellations such as radio astronomical arrays.

A space-based radio astronomical array would operate as a synthetic (phased) array, similar to ground-based arrays, but with the key advantage of not being subjected to distortions introduced by the Earth's ionosphere.All radio astronomical arrays operate on the same principle - pairs of antennas provide a measure of the Fourier transform of the sky (scene) brightness.The key challenge with such arrays are that although only a loose formation is required to obtain the measurements, the relative position of the spacecraft at the time of the measurement must be known. Although real-time knowledge is not needed, meter to sub-meter (depending on the wavelength being observed) knowledge of the spacecraft baselines (i.e., separations) is needed during the science data analysis. The challenges associated with forming such a spacecraft constellation and determining relative position knowledge are discussed in this paper.

To motivate this effort, our initial focus is on a space-based array designed to image the radio emission associated with coronal mass ejections (CMEs) from the Sun. The motivation for this focus is two-fold. First, the radio emission from CMEs is a direct tracer of the particle acceleration in the inner heliosphere and potential magnetic connections from the lower solar corona to the larger heliosphere: these questions are among those highlighted in the Solar Decadal Study.[2] Second, CME radio emission is quite strong such that only a relatively small number of antennas is required, and a small mission would make a fundamental advancement. Indeed, the state-of-the-art for tracking CME radio emission is defined by single antennas (Wind/WAVES, Stereo/SWAVES) in which the tracking is accomplished by assuming a frequency-to-density mapping.

In addition to having many astronomical uses, radio arrays are useful in helping us understand various solar processes. Although there are a number of solar observations that can be made from the ground, these measurements have a cut-off around 15 MHz due to the density of the ionosphere. Single instruments on spacecraft such as WAVES on Wind have measured various solar dynamics such as coronal mass ejections (CMEs) and associated Type II and III Bursts, which all give off telltale radiation in the radio range under 15 MHz. These observations could give us early warning of an incoming CME or solar energetic particle event, and they could also help observe CMEs in the disk of the sun, which other instruments such as coronagraphs are unable to capture. In parallel, recent development in CubeSat technology have shown that low cost orbiting radio receivers are feasible. Consequently, the next step would be to launch a number of radio receivers to create an interferometer, thus enabling higher sensitivity images of CME structure. Such an interferometer would have the advantage of not being coplanar, a geometry that cannot be achieved on Earth.

The details of the science motivation behind such an array, along with the spacecraft and payload design is the subject of a separate paper [11]. Table 1 presents the key driving requirements that such an array would have on the spacecraft cluster design and operation. These are the requirements which are used for the remainder of this paper.

3. FORMATION DESIGN STRATEGY

The performance of the space-based radio interferometer is inextricably linked to the relative motion of the spacecraft composing the formation. Accordingly, we discuss the details of the design strategy, including: (i) our use of natural relative dynamics to alleviate the need for active formation control; (ii) useful proxies for characterizing the ability of the array to reconstruct the target radio emissions; and, (iii) a heuristic search method to discover high-performing formation designs.

Dynamical Systems Theory

Any formation design strategy must begin with a method to predict and analyze both the absolute as well as relative motion of the spacecraft. The astrodynamics literature contains numerous such schemes, though most are based upon one of three basic principles:

- perturbations of conic elements or other representations of

[2] "Discover and characterize fundamental processes that occur both within the heliosphere and throughout the Universe."

Table 1. Driving Science Requirements and Derived Mission Design Parameters

Science Requirement		Mission Design Parameters
6 months baseline science operations	*Mission Duration*	8 months including checkouts and calibrations
Electrically short dipole antennas in view of Sun	*Spacecraft Attitude*	Sun-pointed
Observations above Earth's ionosphere	*Target Orbit* *Launch Vehicle*	GEO Altitude Secondary payload / rideshare
Minimum of 5 spacecraft	*Formation Size*	6 spacecraft
In plane perpendicular to Sun-spacecraft line: Maximum separation $\geq$ 10-km; Minimum separation $\leq$ 1-km	*Formation Shape*	Design initial relative orbits such that separation of spacecraft in plane normal to Sun-spacecraft vector varies from 0.5-km to 12-km over the orbit
17-ns relative position and timing uncertainties between spacecraft pairs	*Relative Position Knowledge*	<3-m

orbital motion [12];
- the Clohessy-Wiltshire equations of relative motion [13]; or,
- application of dynamical systems theory (DST) [14];

see Alfriend et al. for a general treatment of the first two methods [3]. Note that for the two-body dynamical model we consider, all three design strategies can produce equivalent relative motions given the correct assumptions and selection criteria. However, we make use of DST for our investigation due to its general flexibility when performing trade studies of close proximity formations: the underlying dynamical regime and baseline orbit can be freely exchanged without need to extensively modify other portions of the design process.

The underlying basis for DST is the linearization of motion around a baseline trajectory, in our case periodic, circular motion about the Earth; see Table 2 for our notional orbital characteristics.[3] Since we operate in the relatively benign

Table 2. Baseline Orbit Parameters

Parameter	Value	Units
Altitude	37021	km
Eccentricity	0	–
Inclination	0	deg.
Period	25	hours

dynamical environment of the GEO graveyard, short-term motion of the satellites is adequately described using Keplerian motion

$$\ddot{\boldsymbol{r}} = \frac{\partial U}{\partial \boldsymbol{r}} \tag{1}$$

where $\boldsymbol{r} = [x, y, z]^T$ and the potential function is given by

$$U^* = \frac{\mu_\oplus}{r} \tag{2}$$

with position magnitude $r = \sqrt{x^2 + y^2 + z^2}$ and Earth's gravitational parameter $\mu_\oplus = 398600.4418 \frac{km^3}{s^2}$. For mathematical convenience, we non-dimensionalize the equations of motion by $\mu_\oplus$ and the radius of Earth, $R_\oplus = 6378.14km$, resulting in the characteristic time $t^* = \sqrt{\frac{R_\oplus^3}{\mu_\oplus}}$ and the new potential function

$$U = \frac{1}{r}. \tag{3}$$

Motion relative to a reference trajectory is linearized as

$$\dot{\boldsymbol{x}} = \boldsymbol{A}(t)\boldsymbol{x} \tag{4}$$

with state vector $\boldsymbol{x} = [x, y, z, \dot{x}, \dot{y}, \dot{z}]^T$ and time-varying linearized dynamic matrix

$$\boldsymbol{A}(t) = \begin{bmatrix} \boldsymbol{0}_{3\times3} & \boldsymbol{I}_{3\times3} \\ \frac{\partial^2 U}{\partial \boldsymbol{r}^2} & \boldsymbol{0}_{3\times3} \end{bmatrix} \tag{5}$$

in an inertial frame. Propagating this linearized motion along a trajectory results in the state transition matrix (STM), $\boldsymbol{\Phi}(t, t_0)$, which maps variations in the initial state to changes in the current state via

$$\delta\boldsymbol{x}(t) = \boldsymbol{\Phi}(t, t_0)\delta\boldsymbol{x}(t_0) \tag{6}$$

with the change in STM given by

$$\dot{\boldsymbol{\Phi}}(t, t_0) = \boldsymbol{A}(t)\boldsymbol{\Phi}(t, t_0) \tag{7}$$

and initial conditions

$$\boldsymbol{\Phi}(t_0) = \boldsymbol{I}_{6\times6}. \tag{8}$$

When the STM is propagated for one period of a closed orbit (i.e., $\boldsymbol{\Phi}(T + t_0, t_0)$), it is also termed the monodromy matrix. Note that Eqs. (4) and (6)-(8) are general dynamical equations valid for any model of orbital motion and Eq. (5) is only altered when the equations of motion are also velocity dependent, for example if they are expressed in a rotating frame.

The STM maps differences in the initial conditions along the resulting perturbed paths and contains information about the underlying dynamical system. In particular, the monodromy matrix reveals the fundamental relative motions of the associated periodic orbit. The eigenvalues γ_i of the monodromy matrix indicate the stability of the orbit while

[3] In principle, higher-order relative motion can be captured, but linearized relative motion suffices for our specific formation design needs.

the associated eigenvectors $\hat{\mathbf{\Gamma}}_i$ can be used to selectively excite the corresponding relative motion. For example, an eigenvalue with magnitude $\|\gamma_i\| > 1$ denotes unstable motion; perturbing the initial state of the period orbit by the step ε in the corresponding eigenvector direction establishes an asymptotic departure from the periodic orbit along the unstable manifold. Variations in the orbital initial conditions due to exciting eigenvalue/eigenvector pairs are expressed as

$$\boldsymbol{x}_0^*(\tau) = \boldsymbol{x}_0(\tau) + \boldsymbol{u}(\tau, \boldsymbol{\theta}, \boldsymbol{\varepsilon}) \tag{9}$$

where τ is a time-like parameter specifying location on the periodic orbit and $\boldsymbol{u}$ is a step into the invariant manifold space. The manifold step for a single eigenvector is [15]

$$\boldsymbol{u}(\tau, \theta_i, \varepsilon_i) = \varepsilon_i \Big(\cos(\theta_i)\Re[\hat{\mathbf{\Gamma}}_i(\tau)] - \sin(\theta_i)\Im[\hat{\mathbf{\Gamma}}_i(\tau)] \Big) \tag{10}$$

where ε_i is the step magnitude, θ_i is an angular parameter, and $\Re$ and $\Im$ denote the real and imaginary components of the complex vector, respectively.[4] By convention, we allow ε_i to encompass both negative and positive values while we restrict θ_i to fall in the interval $[0°, 180°)$.[5] We now generalize the mathematical basis of the manifold step to allow linear combinations of the eigenvectors, that is:

$$\boldsymbol{u}(\tau, \boldsymbol{\theta}, \boldsymbol{\varepsilon}) = \sum_{i=1}^{n} \varepsilon_i \Big(\cos(\theta_i)\Re[\hat{\mathbf{\Gamma}}_i(\tau)] - \sin(\theta_i)\Im[\hat{\mathbf{\Gamma}}_i(\tau)] \Big). \tag{11}$$

Using this formulation, we can selectively excite or suppress components of the local natural flow relative to a baseline orbit, leading to intricate combined manifold motion.

For our orbit in the GEO graveyard, $\|\gamma_i\| = 1$ for all six eigenvalues, indicating dynamical stability and the presence of a multi-dimensional center manifold, or invariant torus [15]. However, of the six eigenvectors, two form a complex conjugate pair and another two are repeated strictly real vectors, this latter phenomenon indicating that the monodromy matrix is degenerate; the remaining two eigenvectors are unique and strictly real. Thus, we can rewrite Eq. (11) as

$$\boldsymbol{u}(\boldsymbol{\varepsilon}, \boldsymbol{\theta}) = \varepsilon_1\hat{\mathbf{\Gamma}}_1 + \varepsilon_2\hat{\mathbf{\Gamma}}_2 + \varepsilon_3\hat{\mathbf{\Gamma}}_3 + \varepsilon_4 \Big(\cos(\theta_4)\Re[\hat{\mathbf{\Gamma}}_4] - sin(\theta_4)\Im[\hat{\mathbf{\Gamma}}_4] \Big) \tag{12}$$

while still retaining the ability to fully exploit the invariant manifold space. Note that we have omitted τ, since we can arbitrarily select a value for τ while still capturing all possible relative formations: our underlying motion is Keplerian and any perturbation at a specific location on the periodic orbit results in perfectly periodic orbits that can be equally realized from any other location on the reference trajectory. In our following analysis, we use $\tau = 0$, the location on the orbit corresponding to $\boldsymbol{x}_0 = [43399km, 0, 0, 0, 3.0306km/s, 0]^T$. Inspecting Eq. (12), we are required to specify only 5 parameters, $[\varepsilon_1, \varepsilon_2, \varepsilon_3, \varepsilon_4, \theta_4]^T$, to generate the 6-element vector defining the initial condition of a perturbed trajectory; regardless of the manifold step taken, some fundamental characteristic of the baseline periodic orbit is preserved. This conserved quantity is the orbital energy, meaning that any perturbed orbit we specify using DST will have the same period as our baseline trajectory; thus, using DST has the additional advantage of automatically preserving our desired passive clustering of the spacecraft.[6] Therefore, to initialize an n-spacecraft passive formation, we need only select values for $5n$ initialization parameters (30 parameters for our nominal formation of 6 spacecraft), that is, $4n$ step magnitudes and n angular offsets.

A Visual Method of Formation Design

While the DST formulation for generating spacecraft formations is quite amenable to automated search strategies, we first wish to gain some insight into the invariant natural flow associated with our mission scenario and test the potential for human intuition in this complex design space. We begin by assessing the behavior exhibited by each eigenvector individually, as illustrated in Fig. 1, where the circles indicate the start of propagation, diamonds $1/4$ of the orbit, triangles $1/2$ of the orbit, and squares $3/4$ of the orbit. Rather than

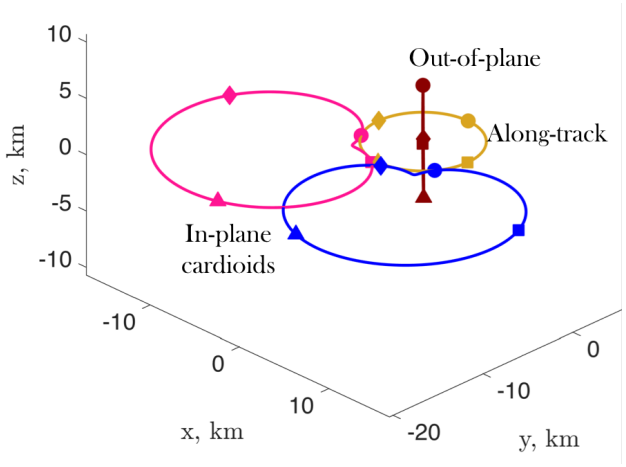

Figure 1. Relative motion arising from exciting individual eigenvectors of the monodromy matrix, shown in axes parallel to equatorial inertial frame axes but centered on the GEO graveyard orbit.

the traditional RTN-frame, we use a set of axes $(\hat{x}, \hat{y}, \hat{z})$ parallel to an inertial, Earth-centered frame, with $\hat{x}$ and $\hat{y}$ in the equatorial plane of Earth, but centered on the GEO graveyard orbit because these quasi-inertial axes are more convenient when assessing the performance of the formation as a Sun-observing interferometer. Two motions are readily identifiable as along-track motion associated with the degenerate repeated eigenvector $\hat{\mathbf{\Gamma}}_1$ and out-of-plane motion represented by the complex eigenvector $\hat{\mathbf{\Gamma}}_4$. The two in-plane motions linked to the strictly real, unique eigenvectors $\hat{\mathbf{\Gamma}}_2$ and $\hat{\mathbf{\Gamma}}_3$ exhibit cardioid relative motion in the quasi-inertial frame. Note that we have generated these relative motions by taking positive steps ε_i; using negative values would produce mirror images across the relevant lines of symmetry. Even this brief inspection reveals behaviors of interest: using the along-track eigenvector produces the well-known "string-of-pearls" formation, while combining the out-of-plane and along-track motions yields elliptical relative motion in the inertially directed axes.

[4] When the eigenvector is fully real, that is, $\Im[\hat{\mathbf{\Gamma}}_i(\tau)] = \mathbf{0}$, the angular parameter θ_i can be set to zero without loss of generality.

[5] It is mathematically equivalent to allow $\theta_i \in [0°, 360°)$ while restricting ε_i to strictly non-negative values.

[6] This behavior is not unique to our particular orbit: the monodromy matrix of any periodic orbit will be deficient, leading to the preservation of an energy-like parameter (energy for two-body orbits, Jacobi constant for restricted three-body orbits, etc.). Bounded motion will not necessarily be preserved for unstable orbits, but the energy-like value will be.

Moving beyond the behavior of the individual manifold steps, we are chiefly interested in how to use Eq. (12) to generate effective linear combinations of the eigenvectors to initialize the formation of spacecraft. To assess the qualitative behavior of candidate relative trajectories we pre-generate sets of linear combinations by sweeping through values for ε_1, ε_2, ε_3 and θ_4, with the resulting manifold steps highlighted in Fig. 2.[7] Each colored sphere represents the attainable space of initial relative positions from a particular combination of three eigenvectors (the remaining step magnitude $\varepsilon_i = 0$), normalized to a step of 10-km. The color of each initial condition is determined by mapping $\pm$ values of the steps ε and $[0°, 180°)$ values of the angular parameter θ to rgb-color channels whereas the size of the marker indicates the maximum excursion from the baseline orbit: larger dots remain closer over the 25-hour period. Each sphere of initial displacements reveals specific concentrations of closely bound relative trajectories, associated with roughly equal but opposite signed steps in the ε_i parameters. The angular parameter θ_4 then affects the phasing within the identified regions. Conveniently, there are 6 of these regions of interest, matching the number spacecraft composing our prospective formation. An intuitive design strategy is then to place one spacecraft in each of these low-excursion regions, for example the prospective formation shown in Fig. 3. The closest spacecraft-spacecraft approach over the course of the 25-hour period is 3.25-km, while the furthest spacecraft-spacecraft recession is 15-km and the maximum relative velocity is 0.75-m/s. However, just because the sample cluster we generated is visually elegant and intuitively obvious doesn't necessarily guarantee good performance when operating as an interferometer; indeed, given the large and complex trade-space presented by the formation design problem, it is exceedingly unlikely that we stumbled upon the optimal design via cosmic coincidence. Thus, an alternate design method is desirable. However, whether we continue using this visually guided design strategy or pursue a more automated approach, we must first develop a metric to evaluate the performance of a particular configuration of spacecraft.

Assessing Formation Performance

Several investigations have examined the optimization of spacecraft formations for interferometric imaging, however common assumptions are either active control and reconfiguration of the formation [16], [17], [18] and/or imaging of a known target object [19], [20]. Thus, specific geometries could be targeted at particular epochs while minimizing the fuel consumption for deterministic maneuvers. In contrast, the goal of our interferometer mission concept is to image radio emissions from solar flare events, which are beyond our current ability to predict accurately. Accordingly, the imaging capability of our spacecraft cluster must be maintained at consistent levels over long durations so that images of the events are captured as they occur. Therefore, we seek a performance metric that evaluates the formation performance over extended periods of time, since our nominal mission spans six months or more.

Our first step in defining the interferometric performance criterion is to evaluate what characteristics of the formation lead to good imaging capability. To observe our target radio frequencies, the spacecraft-spacecraft baselines must fall between 0.5-km and 12-km in separation when projected onto the plane normal to the Sun-spacecraft line, conventionally termed the (u, v)-plane. Further, the baselines must be distributed both in magnitude and angular separation in order to enable reconstruction of the center, size, orientation, and extent of the radio emitting region near the Sun. Combining these criteria, our goal then becomes to scatter the spacecraft-spacecraft baselines across a (u, v)-annulus, as illustrated in Fig. 4; more precisely, we seek to place the projected separations into as many unique bins within the annulus as possible. We have selected the annulus discretization to balance between two extremes: i) too few bins and we will have too many bins filled by more than one baseline; and, ii) too many bins and the baselines may be very close to one another even though they reside in unique bins. Thus, we choose to use 36 bins (3 rings of 12 bins each), or approximately 1.5 times the number of unique baselines (20). Two-sided baselines are highlighted because the interferometric concept we consider can selectively make use of either direction of the spacecraft-spacecraft relative position vector, though not both directions at the same time.

The science annulus is defined in the (u, v)-plane perpendicular to the Sun-spacecraft line, however the Sun-Earth and therefore the Sun-spacecraft direction changes throughout the course of the year. Thus, optimizing the coverage of the passive formation for one particular Sun-line orientation may lead to significantly degraded performance during other portions of the year. To this end, we consider multiple orientations of the (u, v)-annulus as shown in Fig. 5, where the shifting directions approximate the seasonal shifts as Earth orbits the Sun. We only consider the four directions shown because annuli placed in opposite directions will simply yield mirror distributions: the distribution in the respective (u, v)-annulus remains the same whether the Sun-Earth line is parallel or anti-parallel to the $\hat{x}'$-axis. Note that we have now defined a new coordinate system such that $\hat{x}'$ and $\hat{y}'$ reside in the ecliptic plane, a rotation from (x, y, z) of $23.5°$ about the $\hat{x}/\hat{x}'$-axis. The axes remain centered on the GEO graveyard orbit and inertially directed, with $\hat{z}'$ completing the right-hand set. The coordinate set (x'', y'', z'') is defined by a $45°$ rotation from (x', y', z') about the $\hat{z}'/\hat{z}''$ axis.

For the sample formation highlighted in Fig. 3, snapshots of the resulting projected baselines are shown in Fig. 6. For the purposes of illustration we select three epochs of interest, equally spaced around the 25-hour orbit, and the (u, v)-plane is chosen to coincide with the local (x', z')-plane. The center and edge colors of the glyphs correspond to the spacecraft pair forming the respective interferometric baseline. Even though the relative configuration alters over time, the baseline distribution consistently covers significant portions of the science annulus. The mean number of unique bins occupied is 19.4, averaged over the 25-hour orbit and the four directions shown in Fig. 5. This value is approximately $2/3$ of the theoretical maximum of 30 bins that could be covered by the 15 double-sided separations between the 6 spacecraft. Achieving this theoretical maximum may or may not be possible using only natural dynamics, but we still desire to improve the human-designed formation or find a better configuration, if feasible.

Formation Design via Particle Swarm Optimization

A variety of optimization techniques could be applied to the optimization of the formation performance, however two key considerations drive our selection of an appropriate scheme. First, the objective described in the preceding discussion is unlikely to have smooth derivatives, severely restricting

[7] We omit the combination $\hat{\mathbf{\Gamma}}_1, \hat{\mathbf{\Gamma}}_2, \hat{\mathbf{\Gamma}}_3$ because all these components of motion are in-plane with the reference orbit and the resulting "sphere" collapses to a visually uninteresting ring, not because this type of motion in lacks value when constructing a formation of spacecraft.

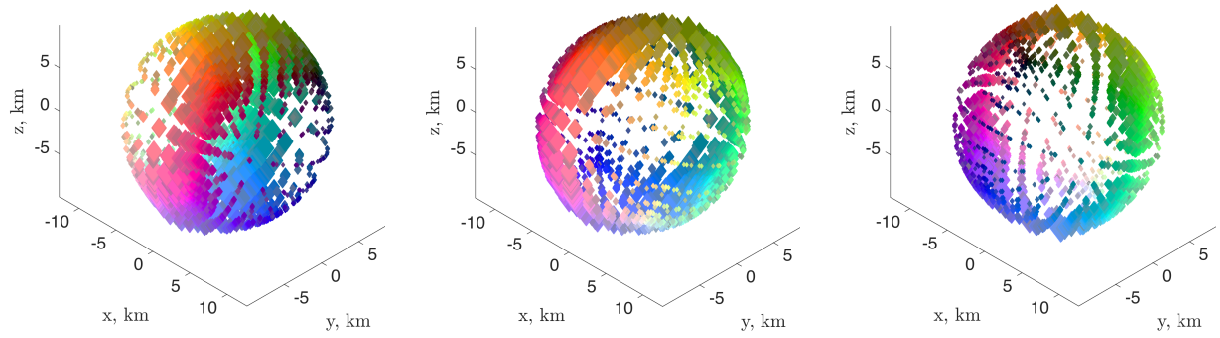

$\varepsilon_1 \rightarrow$ Red, $\varepsilon_2 \rightarrow$ Green, $\theta_4 \rightarrow$ Blue $\varepsilon_1 \rightarrow$ Red, $\varepsilon_3 \rightarrow$ Green, $\theta_4 \rightarrow$ Blue $\varepsilon_2 \rightarrow$ Red, $\varepsilon_3 \rightarrow$ Green, $\theta_4 \rightarrow$ Blue

Figure 2. Spheres of position steps arising from eigenvector combinations, color keys indicate rgb mapping for initialization parameters.

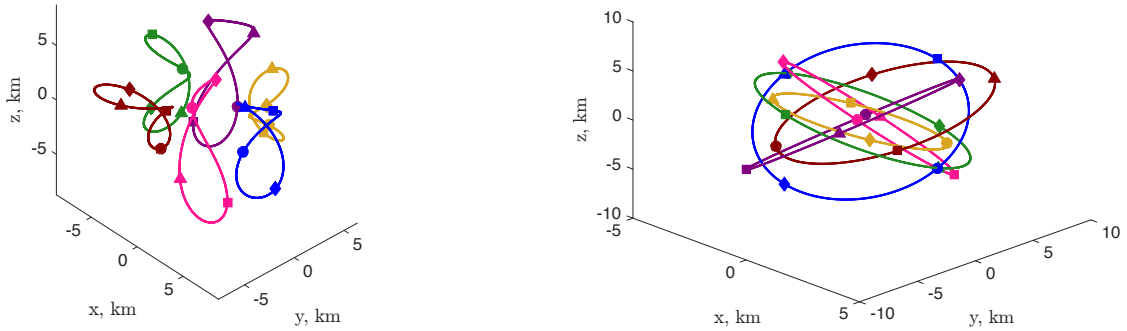

Equatorial inertial axes centered on GEO graveyard Radial-Tangential-Normal (RTN) axes centered on GEO graveyard

Figure 3. Example formation generated using estimated parameters from the initial condition spheres in Fig. 2, xy-plane is equatorial plane of Earth.

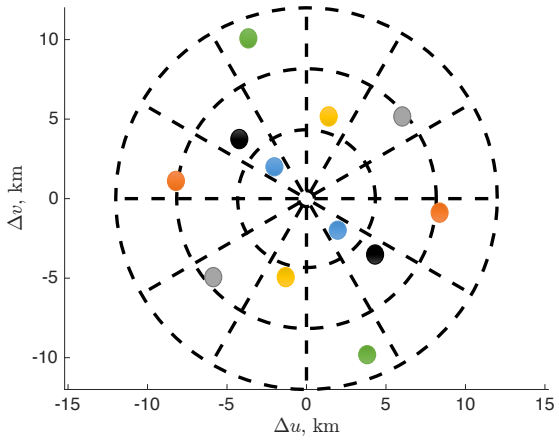

Figure 4. The science annulus in the spacecraft-spacecraft differenced baseline space, with example two-sided separations shown.

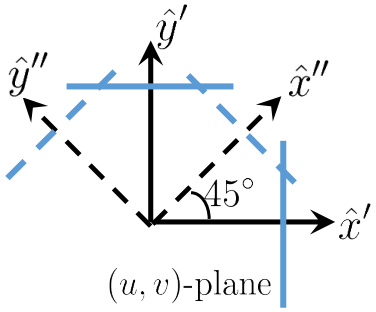

Figure 5. Different projections of the science annulus with respect to the inertially oriented axes.

the utility of gradient-based methods. Second, the global optimization of a constellations presents an extensive and complex trade space for which local optimization methods are not suitable, even when the number of spacecraft is pre-determined. Accordingly we turn to heuristic methods of optimization, specifically particle swarm optimization (PSO) [21], [22], which has been applied in a wide variety of applications [23]. PSO is particularly suitable for our design scenario because of its convenient treatment of continuous variables and global search capability.

PSO operates by mimicking the social behaviors of animals, for example the flocking of birds or the schooling of fish. Agents, or "particles", representing specific designs are distributed throughout a design space, with the subsequent trajectory of each agent through the solution space directed by the behavior and performance of the surrounding agents. The particle swarm is iterated, with updates to the j^{th} agent given by the equation

$$\boldsymbol{X}_j = \boldsymbol{X}_j + \boldsymbol{V}_j \tag{13}$$

with the design vector $\boldsymbol{X}_j$ composed of the DST steps ε and θ for the six spacecraft and the "velocity" term $\boldsymbol{V}_j$ governed

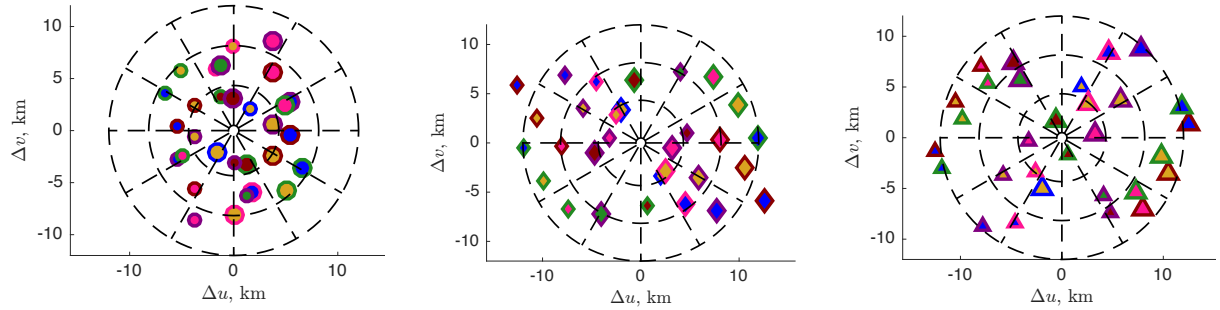

(a) $t = 0$ hrs (b) $t = 8.3$ hrs (c) $t = 16.7$ hrs

Figure 6. Spacecraft-spacecraft baseline snapshots in the projected (u, v)-annulus, visually guided formation design.

by

$$\boldsymbol{V}_j = w_I \boldsymbol{V}_j + w_P \varpi(\boldsymbol{P}_j - \boldsymbol{X}_j) + w_G \varpi(\boldsymbol{G} - \boldsymbol{X}_j). \quad (14)$$

On each iteration, the new velocity is determined by the current $\boldsymbol{V}_j$, the difference from each agent's previous best solution $\boldsymbol{P}_j$, and the difference from the globally best solution $\boldsymbol{G}$ found amongst all the agents. The terms w_I, w_P, w_G are weighting parameters ("inertia", "personal", and "global", respectively) while ϖ represents a value randomly drawn from the uniform distribution over the interval [0,1]. While there are many variations on the basic scheme, our implementation of PSO uses the following steps:

1. A set of agents defining 6-spacecraft configurations is randomly distributed throughout the solution space;
2. All formation designs are evaluated based upon their distribution of the spacecraft-spacecraft baselines, averaged over the 25-hour orbit and the four directions shown in Fig. 5;
3. Each agent's personal best as well as the global best configurations are updated, if necessary;
4. The velocity terms and agent states are updated as defined by Eqs (13) and (14);
5. Repeat Steps 2-4 until a maximum number of iterations is reached.

While the preceding formulation does not necessarily guarantee convergence, solution stability was exhibited for all PSO runs within the maximum number of iterations; that is, the last 10 or so generations led to no improvement in the globally best solution found, $\boldsymbol{G}$.

We apply PSO to two cases of interest: (i) broad searches with no *a priori* knowledge; and, (ii) directed searches seeded by our visually-generated formation design. Recall that our visually guided design strategy limited our solution generation to specific combinations of the monodromy matrix eigenvectors and drove our selection to particular relative orbits. Therefore, we conduct the broad search in order to assess the benefit of relaxing these restrictions and exploring the full solution space. We perform the directed search to evaluate what improvement could be made to the visually intuitive spacecraft cluster. The parameters for the two particle swarm cases are shown in Table 3; the bounds on ε and θ represent intervals over which these values are initialized prior to iteration. For the broad search, random samples are drawn from the uniform distribution between the stated bounds; for the directed run, random samples are drawn from the intervals with the given bounds but centered on the nominal design values from the visually designed formation.

The broad PSO search for formation design results in the relative orbit configurations illustrated in Fig. 7, with projected baseline snapshots in Fig. 9. This formation design results in a mean value of 20.4 bins filled over the 25-hour orbit, with closest spacecraft-spacecraft approach 1.63-km, furthest recession of 18-km, and maximum relative velocity 0.87-m/s. We further note that it is unlikely that a human operator would have discovered this particular cluster design, as the relative orbits do not clearly map back to the set of initial condition spheres shown in Fig. 2. Likewise, the PSO search around the human designed formation results in the trajectories shown in Fig. 8 and (u, v)-annulus coverage plotted in Fig. 10; the closest approach reduces to 3.00-km, the maximum distance is now 13-km, and the maximum relative velocity remains 0.75-m/s. However, the average number of bins occupied is 21.1 over the 25-hour orbit, a clear improvement over the 19.4 from the un-optimized formation. Clearly, the PSO implementation is able to produce high-value formation designs, or improve upon existing ones, while greatly reducing the required effort from human operators.

Table 3. **Parameters for Particle Swarm Runs**

Parameter	Broad	Directed	Units
# Iterations	50	50	–
# Agents	2000	2000	–
Inertia weight, w_I	0.5	0.5	–
Personal weight, w_P	0.5	0.5	–
Global weight, w_G	0.5	0.5	–
ε Bound	[-5,5]	[-0.5,0.5]	km
θ Bound	[0,180)	[-10,10]	deg

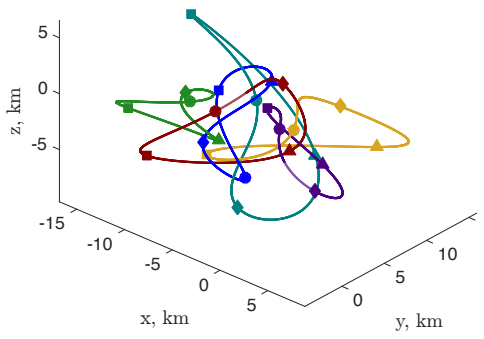

Figure 7. Formation resulting from broad-searching PSO run.

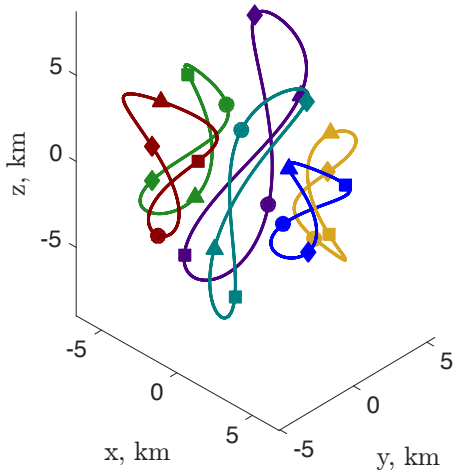

Figure 8. Formation resulting from directed PSO run seeded by visually designed spacecraft cluster.

4. On-Orbit Operations

Once a desired formation configurations has been established, our next step is to assess the operational performance of this design. Two key questions immediately arise:

- How are the spacecraft deployed to their respective orbits?
- How does the passive cluster evolve in the presence of perturbing forces?

To address these concerns, we perform Monte Carlo analysis of a notional deployment case as well as a sample two-week operations interval. Note that in the following discussion, our intent is to establish feasibility, not optimality; for now, it is enough to demonstrate that the proposed formation can be flown safely and with a reasonable ΔV budget.

Formation Deployment

We assume deployment into our target GEO graveyard orbit as secondary payloads on a dedicated GEO communications satellite. Once it deploys the SmallSats, the carrier satellite returns to GEO altitude, leaving the formation flying spacecraft to operate independently. We further assume that we can specify the epoch and direction of ejection from the main bus, within reasonable assumptions on the capability of the main GEO satellite. We assume use of the Canisterized Satellite Dispenser (CSD) for accommodation on the main GEO satellite; the estimated separation velocity is 1.45 m/s [24]. Our deployment strategy for all six spacecraft is a straight-forward three-burn scheme, as depicted in Fig. 11. After a one hour coast following the initial separation from the carrier satellite, a pre-defined stabilization burn is executed to cancel the ejection velocity imparted by the deployment canister. This burn is directed anti-parallel to the assumed initial ejection velocity vector. Three days after the cancellation maneuver, a targeting maneuver is executed to transfer to the destination orbit, followed three days later by the final insertion burn. Three day intervals are chosen to allow adequate collection of navigational data for orbit reconstruction and design times for the maneuvers. The spacecraft are ejected in 60° increments in the plane orthogonal to the inertial velocity of the central GEO graveyard orbit, as demonstrated by the sample deployment shown in Fig. 12. Note that the spacecraft can recede up to a few hundred kilometers from the target cluster before the intermediate targeting maneuver is performed.

While one-off solutions can be readily generated, we are primarily interested in the required Δv budget for the deployment and orbit initialization. Accordingly, we perform a Monte Carlo sensitivity analysis for the stabilization, targeting, and insertion maneuvers. We assume execution and timing uncertainties in the initial ejection and cancellation maneuvers, with nominal and 1-σ uncertainties tabulated in Table 4. We have deliberately selected conservative values

Table 4. **Deployment Monte Carlo Parameters**

Parameter	Nominal	1-σ Uncertainty	Units
Ejection Impulse			
Magnitude	1.45	0.13	m/s
Epoch past $\tau = 0$	180	1	min
Direction	$*$	2	deg
Cancellation Burn			
Magnitude	1.45	0.15	m/s
Coast duration	60	2	min

for uncertainties to account for possible design changes, uncalibrated maneuvers, and the assumed capabilities of the carrier spacecraft. We have neglected uncertainties on the subsequent targeting and insertion maneuvers because the calibrated accuracy of the thrusters is sub-mm/s, well below the other error contributions. A Monte Carlo run of 5000 sample deployments results in the total Δv performance highlighted in Table 5. As we see, the Δv costs for the

Table 5. **Results of Deployment Monte Carlo Run**

SC	Δv	Value (m/s)
Yellow	Mean	3.2199
	1-σ	0.43406
	ΔV-99	4.5221
Blue	Mean	2.6593
	1-σ	0.2742
	ΔV-99	3.4819
Pink	Mean	2.7454
	1-σ	0.4021
	ΔV-99	3.9517
Red	Mean	3.1714
	1-σ	0.41186
	ΔV-99	4.407
Green	Mean	2.6571
	1-σ	0.3061
	ΔV-99	3.5755
Purple	Mean	2.9749
	1-σ	0.3636
	ΔV-99	4.0657

three deployment maneuvers are relatively modest and well within the capability of available SmallSat cold-gas propulsion systems [25]. As expected, the average magnitude of the stabilization burn is commensurate with the ejection impulse. Each satellite splits the remaining Δv cost approximately equally between the targeting and insertion burns, with no consistent pattern on which is larger for any given space-

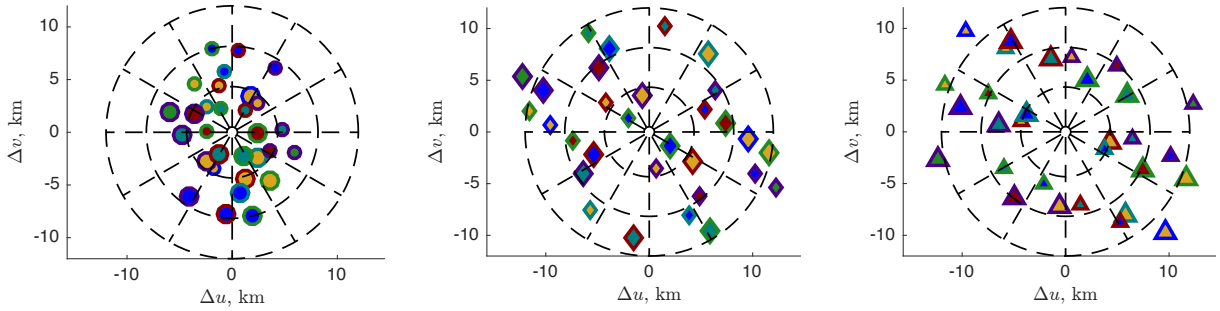

(a) $t = 0$ hrs (b) $t = 8.3$ hrs (c) $t = 16.7$ hrs

Figure 9. Spacecraft-spacecraft baseline snapshots in the projected (u, v)-annulus, broad-searching PSO run.

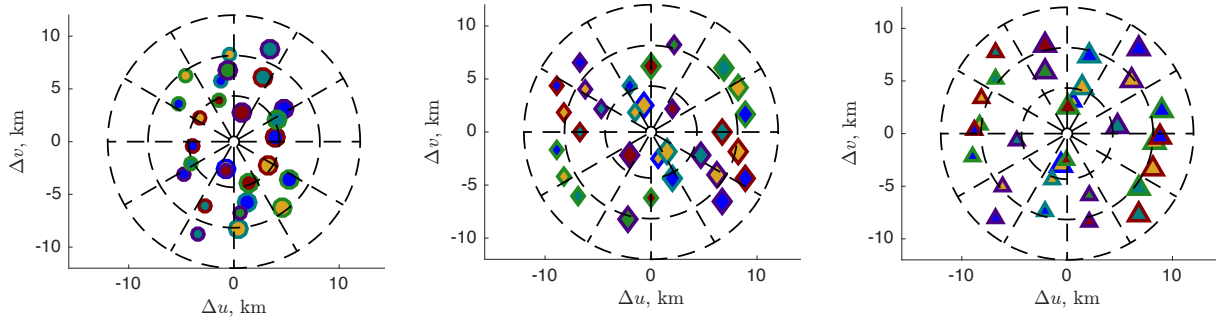

(a) $t = 0$ hrs (b) $t = 8.3$ hrs (c) $t = 16.7$ hrs

Figure 10. Spacecraft-spacecraft baseline snapshots in the projected (u, v)-annulus, directed PSO seeded by visually designed spacecraft cluster.

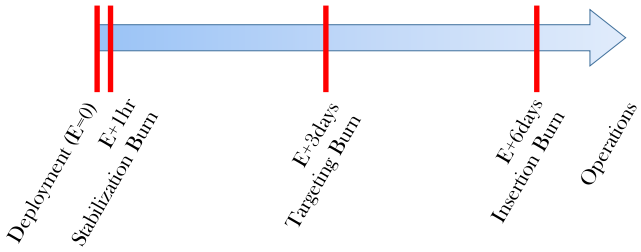

Figure 11. Timeline of spacecraft deployment and insertion into the target orbits.

craft. Thus, while our deployment scheme is not necessarily optimal for this formation configuration, we have at least demonstrated the feasibility of our strategy. As a point of comparison, an investigation in LEO calculated a ratio of total Δv cost to ejection impulse of approximately 4.7, which compares favorably to our derived ratio of 3.1, though their scheme was modified to also explicitly avoid collision risk [26].

Orbit Maintenance

Once the spacecraft have been inserted into their target relative orbits, they enter a quiet observation mode enabling the measurement of radio signals from the Sun. Since the formation will not be actively reconfigured during the nominal mission, the operational goal then becomes maintaining the loose clustering of the spacecraft in their respective trajectories. At GEO altitudes, atmospheric drag is non-existent and gravity effects due to Earth's non-spherical shape are greatly attenuated. Thus, the dominant perturbing terms are multi-body gravity from the Moon and Sun, solar radiation pressure (SRP), and the maneuvers needed to desaturate the spacecraft momentum wheels. While lunar and solar perturbations do cause long-term secular drifts in the inertial orbits, we are not primarily concerned with maintaining precise positioning with respect to Earth, and so only the relative perturbations matter for our application. Likewise, SRP plays an important long-term effect on absolute positioning, but perturbations within the formation are slight because all spacecraft remain actively sun-pointed during the course of normal operations, with attitude perturbations expected to average out over long durations. This leaves only maneuvering as a significant source of short-term perturbations to the relative motion of the spacecraft.

In contrast to gravity and SRP, the desaturation maneuvers are expected to result in significant perturbations to the relative motion of the spacecraft because they are implemented using unbalanced thrusters. Thus, every desaturation event imparts a small Δv to the spacecraft, where this velocity increment slightly alters the relative trajectories of the cluster. Our nominal desaturation strategy is to direct the maneuvers perpendicular to the inertial velocity direction so as to hold the semi-major axis nearly constant. The thrust and velocity vectors are naturally perpendicular twice per orbit because we keep the spacecraft solar panels sun-pointed, and the thrusters are aligned with solar panel normal vector. Thus, implementation of our desaturation scheme is therefore a simple matter of timing the maneuvers for particular epochs. Desaturations are only performed every 3 days, allowing ample freedom in timing the burns appropriately. This straight-forward thrusting law imparts very small changes to the semi-major axis and ensures the orbital period is held nearly constant, thus

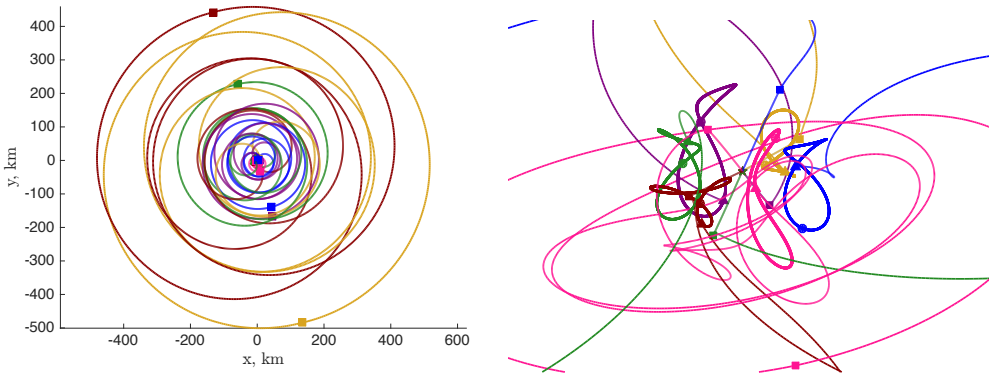

Figure 12. Planar and zoomed views of deployment and relative orbit insertion, in equatorial xyz-frame.

greatly reducing the largest impact on relative drift within the formation.

To assess the viability of our desaturation plan, we perform a Monte Carlo analysis spanning two weeks, or one operational cycle of our passive cluster. Table 6 lists the nominal and uncertainty parameters used for the Monte Carlo analysis; note that we do not consider timing uncertainties because of the nanosecond-level accuracy of the on-board GPS clocks. However, position and velocity errors introduced by the unbalanced maneuvers are not accounted for when implementing subsequent desaturations, reflecting the passive operation of the cluster. Gravitational perturbations from the Sun and Moon are included in the Monte Carlo simulations, along with a flat plate model for SRP and 8×8 spherical harmonics from the Earth. Figure 13 shows a representative perturbed formation over the two-week span, including a trajectory view, a time history of the orbital periods, and a plot of the spacecraft-spacecraft close approaches. As can be seen, small disturbances to the formation period can engender drifts in the relative orbits. On the other hand, close approaches between the spacecraft are still on the order of kilometers and the period discrepancies are readily corrected using a single impulse per spacecraft [27]. A Monte Carlo run of 10,000 samples results in an average corrective Δv of 0.5-mm/s, with a 3-σ value of 1.5-mm/s, to return all spacecraft to the nominal 25-hour period. This prediction is below that for another GEO formation-keeping study [28], though that investigation sought to maintain precise positioning relative to Earth in addition to controlling relative motion. In contrast, a formation-keeping study conducted for LEO predicted Δv magnitudes comparable to ours [29]; this work incorporated atmospheric disturbances to the orbital motion, but did not include perturbations due to momentum desaturation.

Table 6. **Desaturation Monte Carlo Parameters**

Parameter	Value	Units
Magnitude - Nominal	3.2	cm/s
Magnitude - 1-σ Uncertainty	2	%
Pointing - 1-σ Uncertainty	0.33	deg.
Interval between burns	75	hrs

5. Above-the-Belt GNSS Determination

Over the years, GPS has become commonplace for orbit determination in low Earth orbit (LEO). However, using GPS for positioning above the GPS constellation has been less common because the GPS system was designed for terrestrial and LEO users. The GPS transmit antennas point toward the Earth, with no guarantee of reliable signal strength beyond the main beam of the transmitted signal, out to approximately 23 degrees. However, weaker sidelobe signals exist beyond the main beam and can be used for navigation, provided adequate signal-to-noise. A diagram of the transmitted signal structure from the GPS satellites is shown in Figure 14. In order to track satellites, a user in an altitude at or above medium Earth orbit (MEO) would need to rely on acquiring signals transmitted from the opposite side of the Earth from the main beam as well as the sidelobe signals.

Using GPS for orbit determination above the GPS constellation altitude has been a topic of discussion for a number of years, with the one of the first published uses of GPS at GEO presented by Kronman in 2000 [30]. Recent successful uses of GPS at GEO have proved that the GPS L1 frequency can be acquired and tracked for orbit determination purposes at altitudes above MEO. In 2012, Unwin, et al. [31] showed that the SGR-GEO single frequency GPS receiver onboard the GIOVE-A satellite was capable of functioning just beyond MEO by acquiring and tracking GPS satellites. In 2012, Lockeed Martin launched the SBIRS GEO1 satellite with a dual frequency GPS receiver onboard for satellite navigation [32]. Most recently, Winternitz, et al [33] demonstrated on the MMS mission that the GPS L1 signal can not only be tracked above the GPS constellation, but out to an altitude of 12 Earth radii. Furthermore, the upcoming GOES-R satellites plan to do precise orbit determination in GEO strictly via the use of GPS signals [34].

In this paper we propose to use dual frequency global navigation satellite system (GNSS) signals to determine the relative locations of the constellation of the six satellites in the GEO graveyard orbit. In order to overcome the visibility limitations with tracking only GPS, we will use both GPS and GLONASS dual frequency signals to attain meter-level accuracy of the individual spacecraft. The relative positioning required for the interferometer will be computed by simply differencing the orbits to obtain the baseline relative positions.

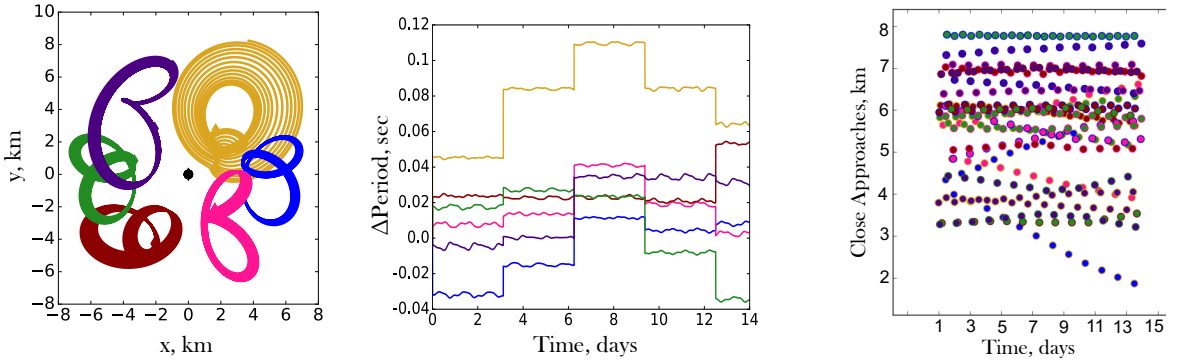

(a) Planar Trajectory View (b) Change in orbital period (c) Spacecraft-spacecraft distances

Figure 13. Formation evolution from a sample two-week on-orbit operations simulation.

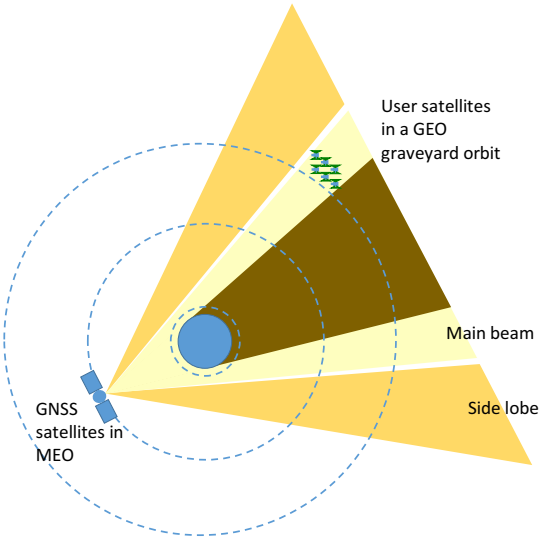

Figure 14. The diagram shows the relative locations of the GNSS satellites to the user satellites in a GEO graveyard orbit. The shaded section shows the blockage from the Earth and the small amount of main beam signal available to a spacecraft at a GEO altitude.

Modeling of spacecraft motion in a GEO Graveyard orbit

In order to simulate the orbital scenario for these six satellites, the GIPSY-OASIS II (GOA-II) software package is used. Developed at JPL, GOA-II has a long history of use for precise orbit determination for scientific missions, including such missions as TOPX-POSEIDON [35], Jason-1 [36], the multiple-antenna COSMIC satellites [37], as well as the tandem-flying GRACE satellites [38]. To simulate the satellites in the GEO graveyard orbit using GOA-II, the spacecraft initial states are input and the orbits are generated over a 30-hour period for each of the satellites. For the transmitter locations, the GPS and GLONASS orbits produced by JPL were used. While the simulations make use of the orbital locations for the GLONASS satellites, the signal characteristics are modeled as GPS satellites. May 19, 2016 was chosen as the date for the analyses, with reconstructed orbital parameters for a total of 54 satellites available. Of these 54 satellites, 31 are GPS satellites and 23 are GLONASS satellites.

In order to accurately simulate the visibility for the satellites, the spacecraft attitude and antenna orientation must be modeled. For the proposed satellites, the antennas are located on opposite faces of the 6U satellite with the antennas on the $+\hat{X}$ and $-\hat{X}$ faces and the solar panels on the $+\hat{Z}$ face, as shown in Fig. 15. Because the solar panels must always be pointing toward the Sun, this constrains the $+\hat{Z}$ spacecraft face to always be pointed in the Sun direction. With this constraint, there are therefore times when the GNSS antennas are not pointed in the Earth-direction. For a given spacecraft position with respect to the Earth, $\vec{p}$, velocity, $\vec{v}$, and Sun direction, $\vec{sun}$, the spacecraft orientation over the orbit is defined using the equations below. First, the spacecraft $+\hat{Z}$ direction is

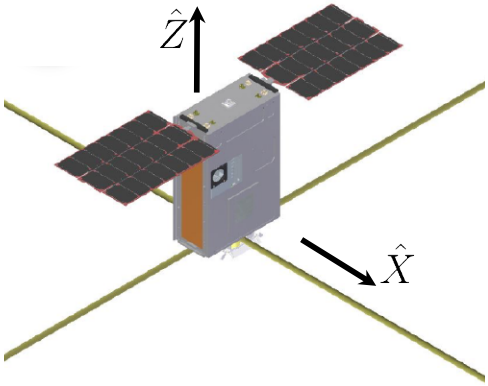

Figure 15. The spacecraft model - 6U satellites with the $+\hat{Z}$ axis pointing toward the Sun and the $\hat{X}$ axes pointed toward the Earth

defined to be aligned with the vector from the Earth to the Sun.

$$\hat{Z} \| \vec{sun} \tag{15}$$

Then, the orbit normal direction, $\hat{n}$, is computed as the normalized cross product of the spacecraft position and velocity.

$$\hat{n} = \frac{\vec{p} \times \vec{v}}{|\vec{p} \times \vec{v}|} \tag{16}$$

To maximize the amount of time that the GNSS antennas are pointed toward the Earth, the spacecraft $\hat{X}$ direction is then computed as the cross product of the normal unit vector with

the spacecraft $\hat{Z}$ vector, and the spacecraft $\hat{Y}$ is defined as the cross product of $\hat{Z}$ with $\hat{X}$.

$$\hat{X} = \hat{n} \times \hat{Z} \tag{17}$$

$$\hat{Y} = \hat{Z} \times \hat{X} \tag{18}$$

When simulating data using the spacecraft attitude and antenna orientations as defined above, the azimuth and elevation of the received and transmitted signals can be computed. Using a local elevation cutoff of 0 degrees on the receiver side and 0 degrees on the transmitter side bounds the total number of satellites available over the 30-hour simulation period, as shown in Figure 16, with an average of 42 satellites visible at any given moment.

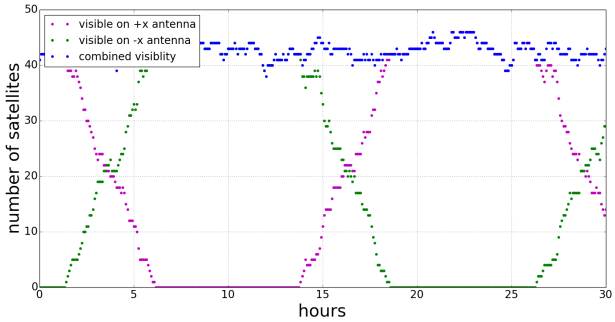

Figure 16. When an elevation cutoff of 0 degrees on the transmitter and receiver satellites is used, an average of 42 satellites are visible over the 30-hour period.

Link Budget Calculation

However, in order to gain a realistic idea of the number of satellites that are capable of being tracked at any given time, we must apply a link budget calculation. For simplicity, the L1 and L2 transmit patterns of the GPS III satellite are used to represent both the GPS and GLONASS satellites [39]. Plots of the L1 and L2 antenna gain patterns are shown below in Figure 17 and 18, while a candidate antenna gain pattern

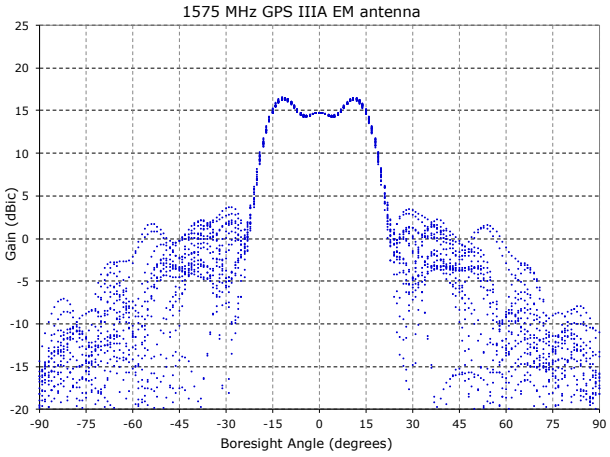

Figure 17. The GPS L1 antenna gain pattern for the GPS III satellites is represented here as a function of off boresight angle (deg) over azimuth angles in increments of 20 degrees.

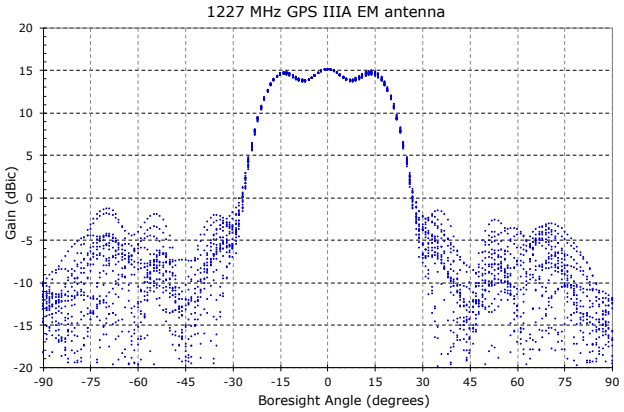

Figure 18. The GPS L2 antenna gain pattern for the GPS III satellites is represented here as a function of off boresight angle (deg) over azimuth angles in increments of 20 degrees.

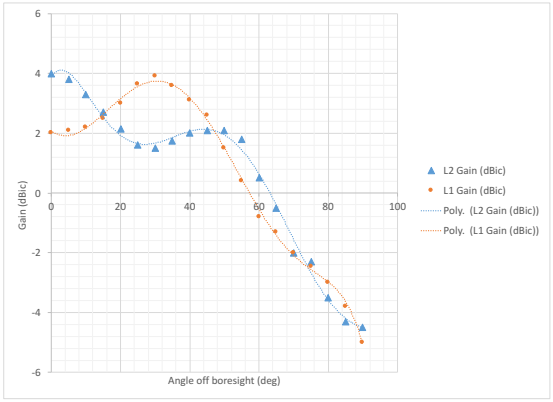

Figure 19. The gain pattern of a candidate GNSS receiver antenna is plotted as a function of offboresight angle, in degrees.

for use on the SmallSats is plotted in Fig. 19. Note that the transmit gain patterns go out to 90 degrees off-boresight, so the main beam as well as sidelobes are considered in the link budget calculation. Azimuthal variations are also considered in the calculations.

For the L1 and L2 frequencies, the received signal strength is computed as follows:

$$S_{recL1} = \frac{P_{xmitL1} G_{xmit} G_{recL1}}{L_{cable}} \left(\frac{\lambda_{L1}}{4\pi R} \right)^2 \tag{19}$$

$$S_{recL2} = \frac{P_{xmitL2} G_{xmit} G_{recL2}}{L_{cable}} \left(\frac{\lambda_{L2}}{4\pi R} \right)^2 \tag{20}$$

where S_{recL1} and S_{recL2} are the received signal strengths, $PxmtL1$ and $PxmitL2$ are the transmit power, $GXmitL1$ and G_{XmitL2} are the transmitter gain patterns toward the spacecraft, G_{recL1} and G_{recL2} are the received antenna gain patterns toward the GNSS satellite, L_{cable} is the cable loss, and $\left(\frac{\lambda_{L2}}{4\pi R}\right)^2$ is the space and efficiency loss.

The simulations assume a GNSS receiver based on JPL's Cion and TriG GNSS receivers [40]. Tracking of GNSS L1 and L2 signals expected in the proposed GEO graveyard orbit is feasible, as demonstrated in the GRAIL experiment in 2012 [41]. Based on tests during this experiment, a receiver of this type is capable of acquiring a signal with a strength of 30 dB, and can maintain lock on a signal at the 25 dB level. Using the link budget calculation for both the L1 and L2 frequencies, as shown in equations 19 and 20, the resulting number of satellites over the 30-hour simulation period is shown in Fig. 20 for the times when both the L1 or L2 signals are available, averaging to 8.6 satellites over the 30-hour period. For consistency, thresholds of 30 dB for acquisition and 25 dB for lock maintenance where used when generating Fig. 20.

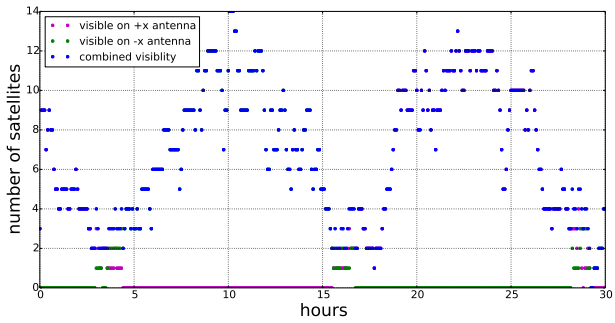

Figure 20. When an elevation cutoff of 0 degrees on the transmitter and receiver satellites is used, an average of 8.6 satellites are above the acquisition cutoff at the start of track and above the tracking threshold at end of track over the 30-hour period.

Simulated Errors

In order to include the expected errors on a small satellite of this type in a GEO graveyard orbit, several types of errors were considered. Because of the high altitude and compact formation, errors in gravity models will not be very pronounced. However, the dynamic modeling errors related to solar radiation pressure will be distinct for each of the six spacecraft.[8] Solar radiation pressure modeling errors were injected by simulating data with attitude errors of 1 to 3 degrees in each axis as well as erroneous sizes for the spacecraft faces that differ for each satellite from truth by 10 to 20%. In addition to errors related to solar radiation pressure, GNSS orbit error was modeled and noise was added to all of the data at a level of 5-meters for pseudorange and 5-cm for carrier phase. Since our orbit reconstruction simulation covers one 30-hour interval, we omit errors introduced due to desaturation events; in practice, these disturbances can be characterized as part of the normal orbit determination process.

Simulation Results

Once the simulated signals have been created for the six small spacecraft, the data are then processed using GOA-II. When processing the simulated data, the truth attitude and spacecraft which were generated with errors in the attitude and spacecraft surface modeling, the truth attitude is used, as well as the truth spacecraft panel models. Generating the simulated data with the attitude and surface modeling errors in place, and then processing with the assumed truth values mirrors the situation that would happen operationally. To process these data, a reduced dynamic orbit determination strategy is used [42]. A reduced dynamic orbit strategy is one in which empirical accelerations are estimated in order to account for unmodeled accelerations, such as mismodeled solar radiation pressure or drag. Because the orbit modeling errors at this high altitude do not contain significant accelerations from forces such as drag, which are difficult to accurately model, the reduced dynamic orbit determination strategy here relies heavily on the well-known dynamics of the orbit, and less so on strength of the relatively-noisy measurement data.

The orbit error associated with processing the simulated data for two satellites positioned independently is shown in Figure 21. Because of the common errors between the two satellites, the relative error decreases when the baseline is formed between the two satellites, as shown in Figure 22. The average root mean square (RMS) error for the six satellites is 1.08-m in 3D position and 3.5-ns for clock error; these clock and relative ranging uncertainties satisfy the required knowledge accuracy for the interferometric mission concept, as stated in Table 1.

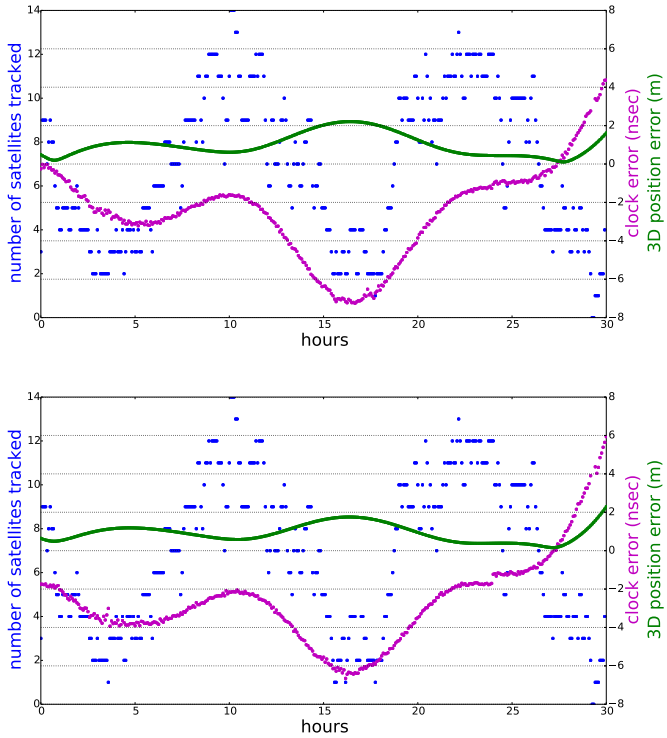

Figure 21. The orbit error for a single satellite has a 3-D RMS of 1.14-m for Yellow satellite (top) and 1.02-m for Pink satellite (bottom).

6. Relative Positioning via UHF Crosslinks

An alternative strategy to meet the relative position knowledge requirement has been formulated based on measurements of the range and bearing between the spacecraft. For

[8]We distinguish between *perturbations* that affect the long-term evolution of the formation and *modeling errors* that reduce the short-term accuracy of orbit reconstructions. Accordingly, SRP may not dominate in terms of station-keeping, but remains an important factor in orbit determination.

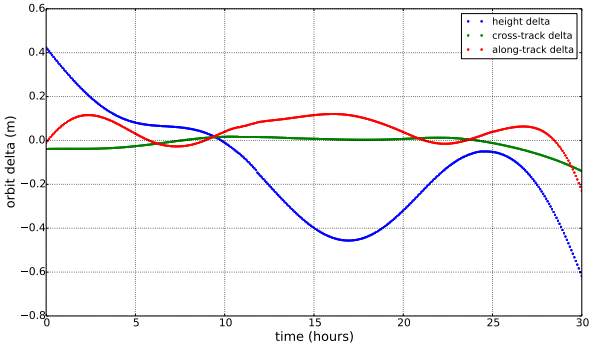

Figure 22. The relative orbit error for a baseline between Yellow and Pink satellites has a 3-D RMS of 0.51-m.

this scheme, each spacecraft will carry a ultra-high frequency (UHF) radio which can measure spacecraft-to-spacecraft range. Moreover, each spacecraft will carry a star tracker, a camera that can measure the orientation of each spacecraft with respect to the distant stars. The same camera can be used to track a light-emitting diode (LED) attached to the outside surface of each spacecraft in the formation. By looking at these LEDs, the star trackers can measure spacecraft-to-spacecraft bearing (right ascension and declination) with respect to an inertially aligned reference frame.

Crosslink Tracking Schedule

By locking-on the UHF radios of two different spacecraft, for example, Yellow and Blue from Fig. 3, the range between these two spacecraft can be measured. It takes approximately 9 minutes to lock-on two UHF radios. Once they are locked-on, the range between the spacecraft can be measured every second. However, to subsequently measure the range between Yellow and another spacecraft, say Pink, the UHF radios of Yellow and Pink need to be locked-on, which will take again 9 minutes. Likewise, by pointing the camera of one spacecraft to another spacecraft, for example, if Yellow points its camera to Blue, Yellow can measure the bearing of Blue with respect to an inertially aligned reference frame centered at Yellow. Once Yellow is pointing to Blue, the bearing of Blue can be measured every second. However, if Yellow then wants to measure the bearing of Pink, it will have to perform an slew to point to Pink, which will take time and perturb the orbit by introducing relative dynamics due to differences in solar pressure as well as a potential increase in the number of desaturation maneuvers.

Scheduling the range and bearing measurements between the spacecraft is not trivial. One point to consider when defining this measurement schedule is that if the range and bearing between two spacecraft are measured at the same time, this is equivalent to an instantaneous measurement of the relative position vector between these two spacecraft, which is the variable we are trying to estimate. If the range and bearing between two spacecraft are taken at different times, explicitly or implicitly, the filter will have to rely on some model of the orbital dynamics to estimate the relative vector from these asynchronous measurements. Hence, it is preferable to have synchronous range and bearing measurements between two spacecraft. Another point to consider is that to have similar relative position knowledge between every two spacecraft, the measurement schedule should foresee range and bearing measurements between every two spacecraft. Unfortunately, this implies frequent attitude slews.

Based on these two points, we suggest the measurement schedule specified in Table 7. This measurement schedule repeats every 50 minutes. This is the minimum time required to measure the range and bearing between every two spacecraft in the formation using the sensors described previously. The table shows the time intervals during which synchronous range and bearing measurements are taken, with a frequency of 1 Hz. It also shows how the different spacecraft are interlocked during these time intervals.

Table 7. **Measurement schedule, where t_0 is the starting epoch and $k \in \mathbb{Z}^+$.**

Time Interval, min	Pairs
$[t_0 + 9 + 50k, t_0 + 10 + 50k]$	Yellow - Blue Pink - Red Green - Purple
$[t_0 + 19 + 50k, t_0 + 20 + 50k]$	Yellow - Pink Blue - Green Red - Purple
$[t_0 + 29 + 50k, t_0 + 30 + 50k]$	Yellow - Red Blue - Purple Pink - Green
$[t_0 + 39 + 50k, t_0 + 40 + 50k]$	Yellow - Green Blue - Red Pink - Purple
$[t_0 + 49 + 50k, t_0 + 50 + 50k]$	Yellow - Purple Blue - Pink Red - Green

Simulation Setup

A simple simulation was put together to demonstrate the feasibility of this strategy. The true motion of the formation is simulated by numerically propagating the initial conditions, designed with the visually aided strategy, using a point-mass gravitational model and a constant exogenous acceleration,

$$\dot{r}^I_{j/I} = v^I_{j/I}, \tag{21}$$

$$\dot{v}^I_{j/I} = -\mu_\oplus \frac{r^I_{j/I}}{\|r^I_{j/I}\|^3} + a^I, \tag{22}$$

where $r^I_{j/I}$ is the position of spacecraft j, $j = 0, ..., 5$, with respect to the (origin of the) Earth-Centered-Inertial (ECI) frame expressed in the ECI frame, $v^I_{j/I}$ is the velocity of spacecraft i with respect to the ECI frame expressed in the ECI frame, and a^I is the constant exogenous acceleration expressed in the ECI frame. The constant exogenous acceleration is a simple proxy for the main perturbing accelerations at GEO. It is defined as $a^I = 10 \times 10^{-6} \frac{[1\ 1\ 1]^\intercal}{\sqrt{3}}$ m/s^2. Its magnitude reflects the expected magnitude of the perturbing accelerations at GEO whereas its direction is set arbitrarily. Due to the relatively short simulation time and because we are ultimately interested in the relative positions between the satellites, and not in their absolute positions with respect to the ECI frame, this simple model is sufficient for our feasibility study.

The absolute position/velocity of Yellow (satellite 0) is de-

fined as the reference position/velocity to calculate the relative positions/velocities of the remaining 5 satellites, i.e.,

$$r_{i/0}^{IL} = r_{i/I}^{IL} - r_{0/I}^{IL}, \tag{23}$$

$$v_{i/IL}^{IL} = v_{i/I}^{IL} - v_{0/I}^{IL}, \tag{24}$$

where $i = 1, ..., 5$ and the IL-frame is a frame aligned with the ECI frame but centered at Yellow.

The measurements of the range between satellites k and l, as measured by satellite l, where $k, l = 0, ..., 5$ and $k \neq l$, are simulated through

$$r_{k/l,m} = \|r_{k/l}^{IL}\| + v_{r_{k/l}}, \tag{25}$$

where

$$r_{k/l}^{IL} = r_{k/0}^{IL} - r_{l/0}^{IL} \tag{26}$$

and $v_{r_{k/l}}$ is a zero-mean discrete-time Gaussian white process with variance

$$E\left\{v_{r_{k/l}}(t_1)v_{r_{k/l}}^{\intercal}(t_2)\right\} = (1/3)^2\delta_{t_1t_2}\ \text{m}^2. \tag{27}$$

On the other hand, the bearing measurements are divided in right ascension and declination measurements. The measurements of the right ascension of satellite k as seen by and measured by satellite l are simulated through

$$RA_{k/l,m} = \text{atan2}\left(r_{k/l}^{IL}(2), r_{k/l}^{IL}(1)\right) + v_{RA_{k/l}}, \tag{28}$$

where $v_{RA_{k/l}}$ is a zero-mean discrete-time Gaussian white process with variance

$$E\left\{v_{RA_{k/l}}(t_1)v_{RA_{k/l}}^{\intercal}(t_2)\right\} = 35^2\delta_{t_1t_2}\ \text{arcsec}^2. \tag{29}$$

The measurements of the declination of satellite k as seen by and measured by satellite l are simulated through

$$DE_{k/l,m} = \text{asin}\left(\frac{r_{k/l}^{IL}(3)}{\|r_{k/l}^{IL}\|}\right) + v_{DE_{k/l}}, \tag{30}$$

where $v_{DE_{k/l}}$ is a zero-mean discrete-time Gaussian white process with variance

$$E\left\{v_{DE_{k/l}}(t_1)v_{DE_{k/l}}^{\intercal}(t_2)\right\} = 35^2\delta_{t_1t_2}\ \text{arcsec}^2. \tag{31}$$

For every spacecraft interlock specified in Table 7, only the left spacecraft is assumed to be taking measurements. One could also study a scenario where both interlocked spacecraft are taking measurements of the same relative position vector at the same time. The estimation error is expected to decrease in that case.

A simple Extended Kalman Filter (EKF) [43] was implemented to estimate the relative position vectors $r_{i/0}^{IL}$, $i = 1, ..., 5$. This EKF assumes no information is available about the state (position, velocity, and acceleration) of satellite 0 with respect to the ECI frame, not even its mean motion. This is a worst-case scenario as some information is expected to be available about the state of satellite 0 with respect to the ECI, either from GNSS measurements or ground measurements. This analysis thus serves to bound the maximum expected estimation error when the inertial state of satellite 0 is unknown. The continuous-time state equations of the EKF are given by

$$\dot{r}_{i/0}^{IL} = v_{i/IL}^{IL}, \tag{32}$$

$$\dot{v}_{i/IL}^{IL} = a_{i/IL}^{IL}, \tag{33}$$

$$\dot{a}_{i/IL}^{IL} = w_i, \tag{34}$$

where $i = 1, ..., 5$ and w_i is a zero-mean Gaussian white process with covariance

$$E\left\{w_i(t)w_i^{\intercal}(\tau)\right\} = Q\delta(t-\tau) = qI_3\delta(t-\tau). \tag{35}$$

Hence, between measurements, the EKF propagates the relative states of the spacecraft by assuming the relative accelerations $a_{i/IL}^{IL}$ are constant. Whenever measurements are available, the EKF updates the estimates of $a_{i/IL}^{IL}$. The continuous-time state equations can alternatively be written as

$$\dot{x} = Ax + Gw, \tag{36}$$

where

$$x = [r_{1/0}^{IL}\ ...\ r_{5/0}^{IL}\ v_{1/IL}^{IL}\ ...\ v_{5/IL}^{IL}\ a_{1/IL}^{IL}\ ...\ a_{5/IL}^{IL}]^{\intercal}, \tag{37}$$

$$w = [w_1\ ...\ w_5]^{\intercal}, \tag{38}$$

$$A = \begin{bmatrix} 0_{15\times15} & I_{15} & 0_{15\times15} \\ 0_{15\times15} & 0_{15\times15} & I_{15} \\ 0_{15\times15} & 0_{15\times15} & 0_{15\times15} \end{bmatrix}, \tag{39}$$

$$G = \begin{bmatrix} 0_{15\times15} \\ 0_{15\times15} \\ I_{15} \end{bmatrix}. \tag{40}$$

Because (39) is time-invariant, the discretization of (36) is straightforward. Ultimately, this means that the expected value of x, i.e., $\hat{x}$, can be propagated in time through

$$\hat{x}[k+1] = \mathbf{\Phi}[k+1,k]\hat{x}[k], \tag{41}$$

where the discrete-time state transition matrix is given by

$$\mathbf{\Phi}[k+1,k] = e^{A\Delta t} \tag{42}$$

and Δt is the propagation time step. Likewise, the state covariance matrix can be propagated through

$$P[k+1] = \mathbf{\Phi}[k+1,k]P[k]\mathbf{\Phi}^{\intercal}[k+1,k] + Q_d[k], \tag{43}$$

where

$$Q_d[k] = \int_0^{\Delta t} \mathbf{\Phi}[k+1,k]GQG^{\intercal}\mathbf{\Phi}^{\intercal}[k+1,k]\text{d}t. \tag{44}$$

Both (42) and (44) have exact closed-form solutions.

For the measurement update, the derivatives of (25), (28), and (30) with respect to x must be determined. They can

be formed from

$$\frac{\partial r_{k/l,m}}{\partial r^{IL}_{k/\mathrm{o}}} = \frac{(r^{IL}_{k/l})^{\mathsf{T}}}{\|r^{IL}_{k/l}\|} = -\frac{\partial r_{k/l,m}}{\partial r^{IL}_{l/\mathrm{o}}}, \tag{45}$$

$$\frac{\partial RA_{k/l,m}}{\partial r^{IL}_{k/\mathrm{o}}} = \begin{bmatrix} \frac{-r^{IL}_{k/l}(2)}{r^{IL}_{k/l}(1)^2+r^{IL}_{k/l}(2)^2} \\ \frac{r^{IL}_{k/l}(1)}{r^{IL}_{k/l}(1)^2+r^{IL}_{k/l}(2)^2} \\ 0 \end{bmatrix}^{\mathsf{T}} = -\frac{\partial RA_{k/l,m}}{\partial r^{IL}_{l/\mathrm{o}}}, \tag{46}$$

$$\frac{\partial DE_{k/l,m}}{\partial r^{IL}_{k/\mathrm{o}}} = \begin{bmatrix} \frac{-r^{IL}_{k/l}(1)r^{IL}_{k/l}(3)}{\sqrt{1-\frac{r^{IL}_{k/l}(3)^2}{\|r^{IL}_{k/l}\|^2}}\|r^{IL}_{k/l}\|^3} \\ \frac{-r^{IL}_{k/l}(2)r^{IL}_{k/l}(3)}{\sqrt{1-\frac{r^{IL}_{k/l}(3)^2}{\|r^{IL}_{k/l}\|^2}}\|r^{IL}_{k/l}\|^3}, \\ \frac{r^{IL}_{k/l}(1)^2+r^{IL}_{k/l}(2)^2}{\sqrt{1-\frac{r^{IL}_{k/l}(3)^2}{\|r^{IL}_{k/l}\|^2}}\|r^{IL}_{k/l}\|^3} \end{bmatrix}^{\mathsf{T}} = \frac{\partial DE_{k/l,m}}{\partial r^{IL}_{l/\mathrm{o}}}. \tag{47}$$

The simulation is run for 400 minutes using a fixed-step size of 1 second. This corresponds to 8 repetitions of the measurement cycle described in Table 7.

The EKF is given initial guesses of the relative positions that are 100 m away from the true relative positions in a random direction. The EKF is also given initial guesses of the relative velocities that are incorrect 1 cm/s in a random direction. The initial guesses of the relative accelerations are set to zero. Finally, the initial state covariance is given by

$$P[0] = \begin{bmatrix} (100\text{ m})^2 I_{15} & 0_{15\times15} & 0_{15\times15} \\ 0_{15\times15} & (1\text{ cm/s})^2 I_{15} & 0_{15\times15} \\ 0_{15\times15} & 0_{15\times15} & (0.1\text{ mm/s}^2)^2 I_{15} \end{bmatrix}$$

and the process noise is tuned to $q = (1\times10^{-7})^2\ (\text{m/s}^{3.5})^2$.

Simulation Results

Figure 23 shows the true relative orbits in the IL-frame, a frame aligned with the ECI frame but centered at satellite 0. Then, Figure 24 shows the true and estimated coordinates of the relative positions also expressed in this frame. More importantly, Figure 25 shows the error between the true and estimated relative positions and their 3-sigma bounds, as calculated by the EKF. The filter clearly reaches steady-state after approximately 90 min, i.e., after approximately two repetitions of the measurement cycle. The convergence from the initial relative position errors is perfectly visible in Figure 25, but even more apparent in Figure 26, which shows the norm of the relative position estimation error for each spacecraft.

The RMS errors of the relative position estimates after 200 min (after the filter has converged) are shown in Table 8. Although the RMS error does not exactly satisfy the 3 meter requirement, it is of the same order of magnitude. Again, we remind the reader that the simple EKF presented here does not know anything about the state (position, velocity, acceleration) of satellite 0 with respect to the ECI frame. With this information, the filter could do a much better job propagating the relative positions and this should result in smaller RMS errors. Further analysis is required to determine how well the inertial state of satellite 0 can be estimated and the impact of this information on the estimation of the relative states.

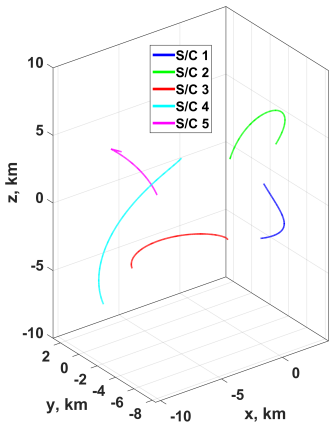

Figure 23. True relative orbits in the IL-frame.

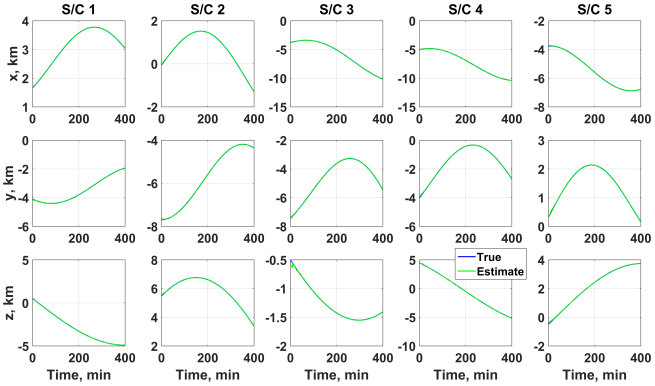

Figure 24. True and estimated relative positions expressed in the IL-frame.

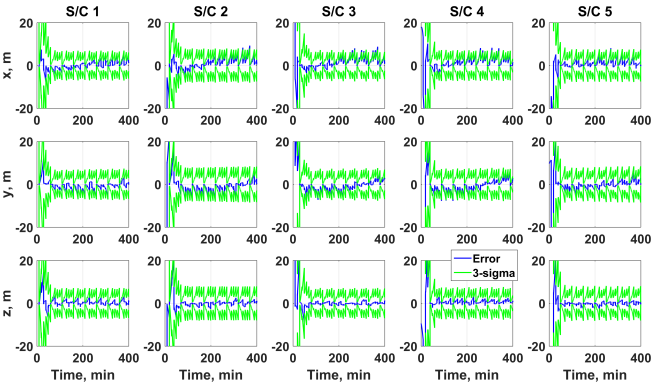

Figure 25. Relative position estimation error expressed in the IL-frame.

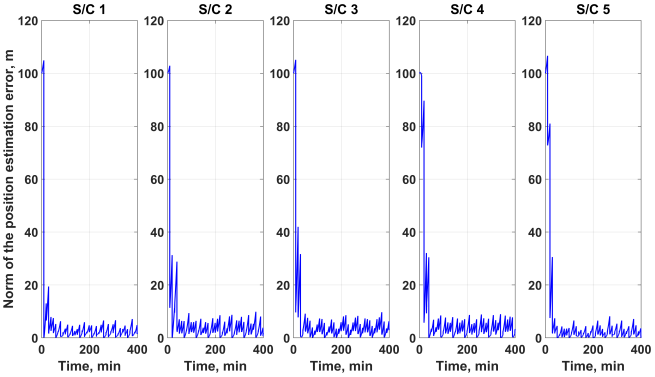

Figure 26. Norm of the relative position estimation error.

Table 8. RMS relative position estimation error after 200 min.

Spacecraft	RMS, m
1 (Blue)	2.8
2 (Pink)	4.1
3 (Red)	4.1
4 (Green)	4.2
5 (Purple)	2.8

7. SUMMARY

In this investigation, we have developed a baseline strategy for the design and operation of a passive cluster of spacecraft forming a space-based interferometer in the GEO graveyard orbit. Our science objective is to image the radio emitting regions associated with coronal mass ejections and other solar events, a task ideally suited for a space-based array loosely bounded on the order of 10-km. The relative orbits comprising the formation are initialized via dynamical systems theory and the linear combination of invariant manifold components associated with a baseline periodic orbit. We implement two distinct design strategies, one based on human visual intuition and another upon the particle swarm optimization algorithm; these schemes can be pursued independently or used in conjunction. Furthermore, we developed a proxy for the imaging performance of the interferometer, enabling the evaluation and construction of high-value spacecraft formations while maintaining relatively rapid solution times. Aspects of the on-orbit operations are considered, namely the initial deployment and ongoing evolution of the array. The Δv cost to initialize the array is on the order of 5-m/s, even for a non-optimized strategy, while subsequent corrections maneuvers are expected on the order of mm/s every few weeks. Precise relative orbit determination is achieved via the use of GNSS signals and ground-based reconstruction techniques, where conservative simulations show that absolute position knowledge is approximately 1-m and spacecraft-spacecraft separation uncertainties are sub-meter over time. An alternate strategy for relative positioning is also explored, wherein UHF crosslinks and star-tracker / LED combinations are used to allow spacecraft-to-spacecraft tracking capability. A simple estimator is readily able to achieve 3- to 4-m accuracy, just at the boundary of the spacecraft-spacecraft position uncertainty allowed for our interferometric concept.

Based upon this work, we offer several observations, as well as avenues for future exploration. First and foremost, above-the-belt GNSS navigation enables this particular mission concept without the need for extensive development of complex inter-satellite networking technologies. On the other hand, more traditional cross-linking approaches to relative orbit determination are still viable, if necessarily more complex and costly. Second, the nature of the target observations permits the use of a passively flying cluster of spacecraft, further simplifying on-orbit considerations and removing the need for on-board autonomy. Third, intuitive deployment and momentum desaturation schemes are operationally feasible and cost-effective while still amenable to further optimization. Fourth, human- and computer-guided design strategies are both independently effective in delivering high-value formation configurations, but show the most promise when use is combined. While this investigation demonstrates the initial feasibility of our mission design and navigation approach, continued work could lead to further improvements. For instance, refinement of the GNSS simulations could lead to increased relative positioning accuracy while optimization of the on-orbit deployment and operations strategies could lead to further improvements in Δv cost and mission safety. Further development of the formation design and UHF cross-linking schemes will help ensure the availability of alternate implementations for the GEO graveyard mission concept as well as potentially enabling alternate mission concepts, for example lunar-centric or deep-space formation missions.

ACKNOWLEDGMENTS

The authors would like to thank the following staff from JPL for their advice and support of our work: Mission Design and Navigation - Ralph Roncoli, Amy Attiyah, Roby Wilson, and Cliff Helfrich; Tracking Systems and Applications - Larry Young, Garth Franklin, and Stephan Esterhuizen; Guidance and Control - Dan Scharf. Without their help, this investigation would have far more difficult and far less enjoyable. The research was carried out at the Jet Propulsion Laboratory, California Institute of Technology, under a contract with the National Aeronautics and Space Administration.

REFERENCES

[1] D.P. Scharf, F.Y. Hadaegh, and S.R. Ploen, "A Survey of Spacecraft Formation Flying Guidance and Control (Part I): Guidance", *Proceedings of the American Control Conference*, Denver, CO, June 4-6, 2003, pgs. 1733-1739.

[2] D.P. Scharf, F.Y. Hadaegh, and S.R. Ploen, "A Survey of Spacecraft Formation Flying Guidance and Control (Part II): Control", *Proceedings of the American Control Conference*, Boston, MA, June 20-July2, 2004, pgs. 2976-2985.

[3] K.T. Alfriend, S.R. Vadali, P. Gurfil, J.P. How, and L.S. Barger, *Spacecraft Formation Flying: Dynamics, Control, and Navigation*, Elsevier, Burlington, MA, 2010.

[4] F. Flechtner, N. Sneeuw, and W.D. Schuh, *Observation of the System Earth from Space - CHAMP, GRACE, GOCE and Future Missions*, Springer-Verlag, Berlin, 2014.

[5] M. Zuber and C.T. Russell (editors), *GRAIL: Mapping the Moon's Interior*, Springer, New York, New York, 2014.

[6] J.L. Burch and V. Angelopoulos (editors), *The THEMIS Mission*, Springer, New York, New York, 2009.

[7] C. Russell and V. Angelopoulos (editors), *The ARTEMIS Mission*, Springer, New York, New York, 2014.

[8] J.L. Burch, T.E. Moore, R.B. Torbert, and B.L. Giles, "Magnetospheric Multiscale Overview and Science Objectives", *Space Science Reviews*, Vol. 199, No. 1, 2016, pgs. 5-21.

[9] S. Bandyopadhyay, G.P. Subramanian, R. Foust, D. Morgan, S.J. Chung, and F.Y. Hadaegh, "A Review of Impending Small Satellite Formation Flying Missions", *Proceedings of the 53rd AIAA Aerospace Sciences Meeting, AIAA SciTech 2015*, January 5-9, 2015, Kissimmee, Florida, Paper No. AIAA 2015-1623. `http://dx.doi.org/10.2514/6.2015-1623`

[10] Keck Institute for Space Studies, "Small Satellites: A Revolution in Space Science", tech. rep., California Institute of Technology, Pasadena, CA, July, 2014. `http://kiss.caltech.edu/study/`

smallsat/KISS-SmallSat-FinalReport.pdf

[11] F. Alibay, J.C. Kasper, T.J.W. Lazio, and T. Neilsen, *Sun Radio Interferometer Space Experiment (SunRISE): Tracking Particle Acceleration and Transport in the Inner Heliosphere*, 2017 IEEE Aersopace Conference Proceedings, Big Sky, MT, 2017.

[12] C.W.T. Roscoe, S.R. Vadali, K.T. Alfriend, and U.P. Desai, "Optimal Formation Design for Magnetospheric Multiscale Mission Using Differential Orbital Elements", *Journal of Guidance, Control, and Dynamics*, Vol. 34, No. 4, 2011, pgs. 1070-1080, DOI: 10.2514/1.52484.

[13] W. Clohessy and R. Wiltshire, "Terminal Guidance System for Satellite Rendezvous", *Journal of the Astronautical Sciences*, Vol. 27, No. 9, 1960, pgs.653-678.

[14] B.T. Barden and K.C. Howell, "Fundamental Motions near Collinear Libration Points and Their Transitions", *Journal of the Astronautical Sciences*, Vol. 46, No. 4, 1998, pgs. 361-378.

[15] Z. Olikara and K.C. Howell, "Computation of Quasi-Periodic Invariant Tori in the Restricted Three-Body Problem", *Journal of the Astronautical Sciences*, Vol. 136, No. 1, 2010, pgs. 313-327.

[16] I.I. Hussein and A.M. Block, "Dynamic Coverage Optimal Control for Interferometric Imaging Spacecraft Formations", *Proceedings of the* 43^{rd} *IEEE Conference on Decision and Control*, Paradise Island, Bahamas, December 2004, pgs. 1812-1817.

[17] I.I. Hussein, D.J. Scheeres, and D.C. Hyland, "Optimal Formation Control for Imaging and Fuel Usage", 15^{th} *AAS/AIAA Space Flight Mechanics Conference*, Copper Mountain, Colorado, January 23-27, 2005, AAS 05-160.

[18] L.D. Millard and K.C. Howell, "Control of Interferometric Spacecraft Arrays for (u,v) Plane Coverage in Multi-Body Regimes", *Journal of the Astronautical Sciences*, Vol. 56, No. 1, 2008.

[19] D.C. Hyland, "Efficient, Passively Orbiting Constellations for High Resolution Imaging of Geosynchronous Objects", *Advances in the Astronautical Sciences*, Vol. 129, No. 1, 2007, pgs. 811-827.

[20] L.D. Millard and K.C. Howell, "Decentralized Optimization for Control of Satellite Imaging Formations in Complex Regions", *Advances in the Astronautical Sciences*, Vol. 134, No. 1, 2009, pgs. 153-171.

[21] J. Kennedy and R.C. Eberhart, "Particle Swarm Optimization", *Proceedings of the IEEE Conference on Neural Networks*, Nov.-Dec. 1995, pgs. 1942-1948.

[22] Y. Shi and R.C. Eberhart, "A Modified Particle Swarm Optimizer", *Proceedings of the IEEE Conference on Evolutionary Computation*, 1998, pgs. 69-73.

[23] R. Poli, "Analysis of the Publications on the Applications of Particle Swarm Optimization", *Journal of Artificial Evolution and Applications*, January 2008, Article No. 4, DOI: 10.1155/2008/685175.

[24] Planetary System Corporation, "Canisterized Satellite Dispenser Data Sheet", http://www.planetarysystemscorp.com/, accessed Oct. 2016.

[25] VACCO, "Propulsion Unit for CubeSats", http://www.vacco.com/images/uploads/pdfs/11044000-01_PUC.pdf, accessed Dec. 2016.

[26] A. Boutonnet, V. Martinot, A. Baranov, B. Escudier, and J. Noailles, "Optimal Circular Formation Initialization with Collision Risk Management", *Advances in the Astronautical Sciences*, Vol. 116, No. 3, 2003, pgs. 2385-2401.

[27] H. Schaub and K.T. Alfriend, "Impulsive Feedback Control to Establish Specific Mean Orbit Elements of Spacecraft Formations", *Journal of Guidance, Control, and Dynamics*, Vol. 24, No. 4, 2001, pgs. 739-745.

[28] V. Kumar, H.B. Hablani, and R. Pandiyan, "Relative Motion Control of Geostationary Satellites in Formation", *Advances in the Astronautial Sciences*, Vol. 145, No. 2, 2012, pgs. 1343-1351.

[29] D. Mishne, "Relative Formation Keeping of LEO Satellites Subject to Small Drag Differences", *Advances in the Astronautial Sciences*, Vol. 109, No. 3, 2001, pgs. 2149-2164.

[30] J.D. Kronman, "Experience using GPS for orbit determination of a geosynchronous satellite", In *Proceedings of the Institute of Navigation GPS 2000 Conference*, 2000, pgs. 1622-1626.

[31] M. Unwin, R. De Vos Van Steenwijk, P. Blunt, Y. Hashida, S. Kowaltschek, and L. Nowak, "Navigating above the GPS constellation - Preliminary results from the SGR-GEO on GIOVE-A", In *Proceedings of the 26th International Technical Meeting of the Satellite Division of the Institute of Navigation (ION GNSS+ 2013)*, Nashville, TN, USA, 2013, pgs. 16-20.

[32] L. Barker and C. Frey, "GPS AT GEO: A FIRST LOOK AT GPS FROM SBIRS GE 01", *Advances in the Astronautical Sciences*, Vol. 144, 2012, pgs.199-212.

[33] L. Winternitz, B. Bamford, S. Price, A. Long, M. Farahmand, R. Carpenter, "GPS Navigation Above 76,000 km for the MMS Mission", *39th Annual AAS Guidance, Navigation and Control Conference*, Feb 8, 2016.

[34] J. Chapel, D. Stancliffe, T. Bevacqua, S. Winkler, B. Clapp, T. Rood, D. Gaylor, D. Freesland, and A. Krimchansky, "Guidance, navigation, and control performance for the GOES-R spacecraft", *CEAS Space Journal*, Vol. 7, No. 2, 2015, pgs. 87-104.

[35] W.I. Bertiger, Y.E. Bar-Sever, E.J. Christensen, E.S. Davis, J.R. Guinn, B.J. Haines, R.W. Ibanez?Meier, J.R. Jee, S.M. Lichten, W.G. Melbourne, and R.J. Muellerschoen, "GPS precise tracking of TOPEX/POSEIDON: Results and implications." *Journal of Geophysical Research: Oceans*, Vol. 99, No. C12,1994, pgs. 24449-24464.

[36] B. Haines, W. Bertiger, S. Desai, D. Kuang, T. Munson, L. Young, and P. Willis, "Initial Orbit Determination Results for Jason-1: Towards a 1 cm Orbit", *Navigation*, Vol. 50, No. 3, 2003, pgs. 171-180.

[37] D. Kuang, W. Bertiger, S. Desai, B. Haines, B. Iijima, and T. Meehan, "Precise orbit determination for COSMIC Satellites using GPS data from two on-board Antennas", *2008 IEEE/ION Position, Location and Navigation Symposium*, 2008, pgs. 720-730.

[38] W. Bertiger, Y. Bar-Sever, S. Bettadpur, S. Desai, C. Dunn, B. Haines, G. Kruizinga et al. "GRACE: millimeters and microns in orbit", In *Proceedings of ION GPS*, 2002, pgs. 2022-2029.

[39] L. Bernard, Private communication, 2009.

[40] T.K. Meehan, "The TriG digital beam steered sounder",

In *2009 IEEE Aerospace*, 2009, doi: 10.1109/AERO.2009.4839464.

[41] S. Esterhuizen, "Moon-to-Earth: eavesdropping on the GRAIL inter- spacecraft time-transfer link using a large antenna and a software receiver", in *25th International Technical Meeting of the Satellite Division of the Institute of Navigation 2012 (ION GNSS 2012)*, Curran Associates, Inc.: Red Hook, NY, 2012, pgs. 2351, ISBN: 978-1-62276-980-3.

[42] T.P. Yunck, W.I. Bertiger, S.C., Wu, Y.E. Bar?Sever, E.J. Christensen, B.J. Haines, S.M. Lichten, R.J. Mueller-schoen, Y. Vigue, and P. Willis, "First assessment of GPS-based reduced dynamic orbit determination on TOPEX/Poseidon", *Geophysical Research Letters*, Vol. 21, No. 7, 1994, pgs. 541-544.

[43] P. Zarchan and H. Musoff, *Fundamentals of Kalman Filtering*, American Institute of Aeronautics and Astronautics, Reston, VA, 2009.

BIOGRAPHY

Jeffrey Stuart *received his B.S., M.S., and Ph.D. in Aeronautics & Astronautics from Purdue University in 2008, 2011, and 2014, respectively. He is currently research staff in Mission Design & Navigation at the Jet Propulsion Laboratory, California Institute of Technology. His interests include automated trajectory design, advanced navigation techniques, combinatorial optimization, and visual analytic methods.*

Angela Dorsey *received her B.S. in Aerospace Engineering from the University of Alabama in 1993, and her M.S. And Ph.D. in Aerospace Engineering Sciences from the University of Colorado in 1995 and 1999, respectively. Her research interests include precise orbit determination for real-time applications as well as GNSS receiver software development.*

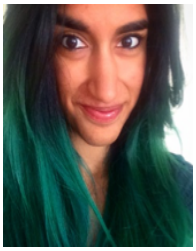

Farah Alibay *received her Bachelor's and Master's degrees from the University of Cambridge in 2010, both in Aerospace and Aerothermal Engineering. She received her PhD in Space Systems Engineering from the Massachusetts Institute of Technology in 2014. Her primary research focused on spatially and temporally distributed multi-vehicle architectures for planetaryexploration. She is now a systems engineer in the mission concept systems development group at JPL, where she works on small spacecraft mission concepts, as well as studies and proposals for larger planetary exploration missions.*

Nuno Filipe *is a GNC Engineer at the NASA/Caltech Jet Propulsion Laboratory. He previously worked for the Control Systems Division of the European Space Agency (2008-2010). Nuno Filipe received a Ph.D. from Georgia Tech, a M.Sc. from TU Delft, and a B.Sc. from Instituto Superior Técnico, all in Aerospace Engineering. He is a recipient of the 2010-2013 International Fulbright Science and Technology Award and of the 2013 Best Graduate Student Technical Paper Award by the AIAA GNC Technical Committee.*